MASTER THESIS

SUPERCONDUCTOR–$Bi_{1.5}Sb_{0.5}Te_{1.7}Se_{1.3}$ TOPOLOGICAL INSULATOR HYBRID DEVICES

Thijs Scholten

FACULTY OF SCIENCE AND TECHNOLOGY
QUANTUM TRANSPORT IN MATTER
INTERFACES AND CORRELATED ELECTRON SYSTEMS

EXAMINATION COMMITTEE
prof. dr. ir. Alexander Brinkman
dr. Stefan Kooij
Marieke Snelder, MSc.

UNIVERSITY OF TWENTE.

26 July 2013

Superconductor-$Bi_{1.5}Sb_{0.5}Te_{1.7}Se_{1.3}$ Topological Insulator Hybrid Devices

Thijs Scholten

26st July 2013

Summary

Topological insulators in proximity to a superconductor and topological superconductors are interesting states of matter, not least because of their potential to host Majorana fermions. Thin flakes of the topological insulator $Bi_{1.5}Sb_{0.5}Te_{1.7}Se_{1.3}$ (BSTS) are studied in Nb-BSTS-Nb junctions of different lengths. These nanojunctions are produced by photo and e-beam lithography and standard sputtering techniques. Four-point transport measurements were performed at temperatures of about 30 mK and in magnetic fields up to 3 T. The smallest two junction were shorted due to an e-beam overexposure, but showed Josephson effects attributed to weak links of Nb ears or microbridges. The observed hysteresis in the I, V-curves of these junctions were attributed to electron heating (hot electrons). Larger junctions (realized junction lengths between 52 and 250 nm) revealed no superconductivity but did reveal interesting resistance peaks at zero bias (ZBRP). These ZBRP are attributed to 2D electron-electron interactions (EEI). The observed side resistance peaks are speculated to be indicative of p-wave induced superconductivity in BSTS. The magnetoresistance was found to be suppressed at lower magnetic fields. This is attributed to weak antilocalization (WAL) (perhaps in combination with EEI). Although the fitting parameters of the 2D HLN-equation deviate from the expected values, the shape does correspond. Several explanations for the deviation are presented.

Additionally, flakes of the topological superconductor $Cu_{0.3}Bi_{2.1}Se_3$ (CBS) are investigated. Samples with gold leads deposited on CBS flakes were manufactured using photolithography and sputter deposition techniques. Four-point transport measurements down to 1.5 K were performed to test if the flakes poses superconductivity. Whereas the bulk crystal was superconducting before and after the measurements on flakes of the same crystal, the flakes itself were not superconducting (resistance in the order of 1 Ω). This is attributed to non-uniform Cu doping by intercalation, giving rise to a small superconducting volume fraction or, possibly, to an easier cleaving of non-superconducting flakes.

Contents

Chapter 1

Introduction

Ever since Kane and Mele [1] in 2005 theoretically proposed the existence of a quantum spin Hall state (or topological insulator), a rapidly growing field in condensed-matter physics has emerged around these so-called topological insulators (TI) [2]. Three years later they predicted, now together with Fu [3], that a Majorana fermion might appear in a superconductor-topological insulator hybrid device. It was realized that the Majorana fermion could be the holy grail for future low-decoherence quantum computing [4, 5]. It is in this perspective that this project on "superconductor-$Bi_{1.5}Sb_{0.5}Te_{1.7}Se_{1.3}$ (BSTS) topological insulator hybrid devices" was initiated.

Although the details of TIs and Majorana fermions will be discussed in the next chapter, a brief introduction of these concepts will be given here for the sake of clarity. A topological insulator is an insulator with metallic surface states, that is, it is insulating in the bulk but at its surface it is necessarily conducting due to its topological nature. Such a material can host a Majorana fermion when it is in proximity to a superconductor [3]. A Majorana fermion is a very unusual particle that is at the same time its own antiparticle, in the present case this would be half an electron and half a hole at the same time. Normally, when a particle and an antiparticle combine, both particles will stop to exists and excite their energy as a photon (light).

1.1 Goal

Previous experimental work on this area at the University of Twente, has focused on hybrid devices of niobium (Nb) and the topological insulator bismuth telluride (Bi_2Te_3) [6, 7, 8]. These devices consisted of Josephson junctions on top of a Bi_2Te_3 flake. In this way a Josephson supercurrent through the topological surface state of Bi_2Te_3 has been shown [8]. This is a first step to pave the way for detecting a Majorana fermion in the superconductor-TI junctions as proposed by Fu and Kane [3].

In this project the goal was to realize a Josephson supercurrent through the surface states of BSTS by Nb-BSTS-Nb Josephson junctions, quite the same as was done in Bi_2Te_3. This switch from Bi_2Te_3 to BSTS is driven by the fact that BSTS overcomes some difficulties that exists in Bi_2Te_3. BSTS has a bulk that is much more insulating than Bi_2Te_3; while the latter has a relatively large bulk carrier density [9]. The surface contribution of Bi_2Te_3 is in the order of 0.3% for a 100 µm thick flake, according to a report by Qu and co-workers [10], this can be contrasted to a realized surface transport in BSTS of about 70% in a 67µm thick flake [11]. Normal bulk carriers destroy the Majorana zero energy mode in the junctions proposed by Fu and Kane [3] (this will be discussed in the next chapter). Therefore, BSTS is a much more promising material compared to Bi_2Te_3.

Aside from this main project, there was a project on copper doped bismuth selenide (Cu-Bi_2Se_3, or short CBS) crystals from the University of Amsterdam. There superconductivity was measured in the crystal. The goal of this project was to verify the expected superconductivity also in Cu-Bi_2Se_3 thin flakes.

1.2 Materials

The material BSTS is a TI, while CBS is expected to be a topological superconductor [20]. If this is indeed true, Majorana fermions would naturally exist in CBS when vortices are present, whereas in BSTS they can only be induced when a superconductor induces superconductivity in the BSTS by the proximity effect. Both materials will be discussed in more detail in the next two sections.

1.2.1 BSTS and its material properties

Already in the sixties alloys of Bi_2Te_3 and Sb_2Te_3 gained some scientific attention, because of their excellent thermoelectric properties near room-temperature [12]. Only in the last few years these materials attained renewed interest, because of their topological nature.

BSTS is a 3D topological insulator (see Chapter 2) with, in the present case, the structural composition of $Bi_{1.5}Sb_{0.5}Te_{1.7}Se_{1.3}$. This is an optimized composition of the topological insulator Bi_2Te_2Se (BTS) in which the Te:Se ratio is reduced and at some positions Bi is replaced by Sb [11, 12]. Still, the ordering of the chalcogen layers is as in BTS [11], see Figure 1.1(a). It was optimized to have maximal bulk resistivity at low temperatures [12] to realize as high as possible relative surface state contribution to the conductance. Taskin [11] and co-workers realized a relative surface transport in BSTS of about 70% in a 67µm thick flake. On much thinner flakes, 200 nm, Xia and collegues [13] realized an even higher relative surface transport of about 99%, at 10 K, but these flakes have a slightly different configuration as the present flakes (Te:Se in 1.8:1.2 instead of 1.7:1.3).

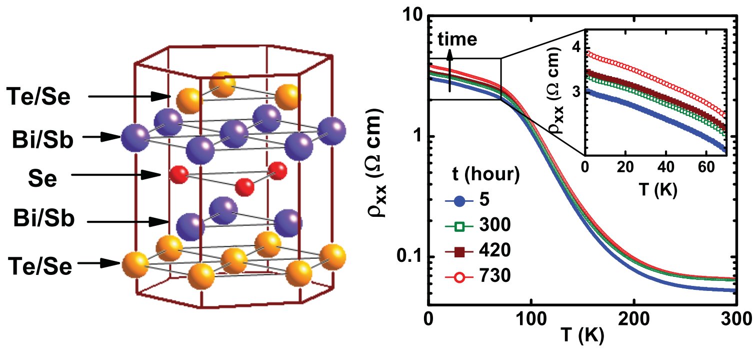

(a) (b)

Figure 1.1: (a) Basic structure unit of $Bi_{1.5}Sb_{0.5}Te_{1.7}Se_{1.3}$ referred to as a quintuple layer. Figure from [11]. (b) $\rho_{xx}(T)$ of a 30 µm cleaved BSTS sample. From 300 K the resistivity increases sharply (insulator behaviour), but it saturates at low temperatures due to metallic surface transport and bulk impurity-band transport [11]. Xia [13] measured even an decrease at low temperatures. Figure from [11]

The BSTS has a layered structure, with a repetition after five layers, referred to as a quintuple layer. The layers within this quintuple layer are strongly bound, while subsequent quintuple layers are much weaker bound – predominantly by Van der Waals bonds [14]. Due to the weak coupling of quintuple layers, a crystal can be easily cleaved in flakes.

BSTS is very sensitive to air exposure, resulting in n-type doping of the surface of BSTS when exposed to air. This effect causes a time evolution of the transport properties of BSTS, after cleaving [11]. Therefore, several measurements on the same sample, not measured at the same time, might give different results, as shown for the resistivity in Figure 1.1(b).

Due to the conducting surface states and the semiconducting bulk of BSTS, the transport properties of BSTS shows semiconductor behaviour at relatively high temperatures, while at low temperatures it saturates or shows even metallic behaviour [11, 13], see Figure 1.1(b). Also a reduction of the bulk results in a larger (metallic) surface contribution in conductivity.

Another prominent property of BSTS is weak antilocalization (see Chapter 2), that becomes clearly visible in a magnetic field sweep around zero field and at low temperatures. As usual, the weak-antilocalization graphs of thin enough flakes can be fitted with the HLN equation with $\alpha = -1$ (or a value close to -1, [13]), if you account for the top and bottom surface of the flake, otherwise $\alpha = -0.5$. A value of $\alpha = 1$ indicates weak localization effects [15]. Also Shubnikov-de Haas oscillations have been observed [11].

The present BSTS crystals were grown by the 'Quantum Electron Matter' group of the University of Amsterdam, by a modified Bridgman method [12, 11, 16].

1.2.2 $Cu_xBi_2Se_3$ and its material properties

The Cu doped topological insulator Bi_2Se_3, giving $Cu_xBi_2Se_3$ (CBS), is recently shown to be superconducting below approximately $T_c = 3.8$ K [17]. It was shown to be a (topological[1]) type II p-wave superconductor, as long as the copper fraction stays within $0.1 \leq x \leq 0.6$, and the copper atoms are intercalated between the Se layers instead of randomly substituting Bi [17, 18]. Whether or not Cu^{1+} is mostly intercalated or mostly added as a substitute strongly depends on the exact growth process, generally both situations are present in the crystal [17], leading to superconducting and non-superconducting regions of the material [19]. The crystal structure of superconducting Cu^{1+} intercalated Bi_2Se_3 according to Hor et al. [17] is shown in Figure 1.2, here one can clearly see that the copper intercalates between the quintuple layers of Bi_2Se_3.

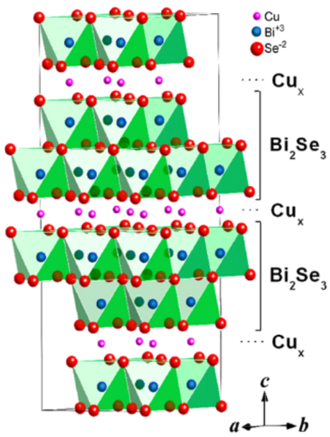

Figure 1.2: The crystal structure of Cu intercalated CBS. Figure from [17].

The growing of CBS consists of melting stoichiometric mixtures of its components in a procedure described in [17, 18]. The flakes used in the measurements discussed in this

[1] $Cu_xBi_2Se_3$ is proposed to be a candidate topological superconductor [20]. In a recent experiment, in a not yet published article [21], this is called into question. This shows that there is still a discussion whether or not it is a topological superconductor.

chapter, were cleaved from a crystal with the composition $Cu_{0.3}Bi_{2.1}Se_3$ and was provided by the University of Amsterdam.

1.3 Outline

The second chapter of this thesis will focus on reviewing the theoretical background for the experiments discussed in the subsequent chapters. In the third chapter the manufacturing of the hybrid devices with Nb-BSTS-Nb junctions, Nb-BSTS-Au junctions and CBS samples will be discussed. The subsequent three chapters, will discuss the experiments on these devices. In the first of these, chapter 4, deals with measurements of shorted Nb-BSTS-Nb junctions, whereas chapter 5 deals with the resistive Nb-BSTS-Nb junctions on the same samples, and shortly the Nb-BSTS-Au samples. Chapter 6 is a short discussion of the results on the transport measurements on CBS samples. This thesis ends with an overview of the conclusions and recommendations for future research (chapter 7).

Note that in this thesis SI-units are assumed, unless otherwise stated.

Chapter 2

Review of theoretical concepts

In this thesis the interaction between a topological insulator and a superconductor is studied. These hybrid systems are interesting in itself because of their special properties, but they can also play an important role for future robust quantum computation, because the system is expected to host Majorana fermions [35, 34].

In this chapter the relevant theoretical background is reviewed, in order to provide a theoretical context for the experiments discussed in later chapters.

2.1 Superconductors

Superconductors are materials that exhibit the extraordinary property that below a critical temperature T_c, resistance disappears and magnetic fields become expelled from the material (the so-called Meissner-effect). Also the current(density) applied through the superconductors as well as the magnetic field over the superconductor, need to be below a certain critical value.

Two types of superconductors can be distinguished: type-I and type-II superconductors. In contrast to the first, the latter has an intermediate critical field B_{c1}. If $B \geq B_{c1}$ normal regions enter the superconductor as normal-core vortices which coexists with the superconductivity.

In a BCS superconductor interactions of the electrons with the lattice give rise to the formation of Cooper pairs. In conventional s-wave superconductivity, Cooper pairs consist of two electrons with a total spin of zero, since they have opposite spin projections ($\uparrow\downarrow$ or $\downarrow\uparrow$) forming a spin-singlet: $\frac{1}{\sqrt{2}}(\uparrow\downarrow - \downarrow\uparrow)$. The exotic p-wave superconductivity has, on the other hand, a total spin of one, with equal spin projections ($\uparrow\uparrow$ or $\downarrow\downarrow$) forming the triplet pairing [5] (which also includes the possibility of $\frac{1}{\sqrt{2}}(\uparrow\downarrow + \downarrow\uparrow)$).

In this section some more key properties of superconductors, necessary to understand the experiments, will be discussed.

2.1.1 Junctions and the Josephson effect

Consider the following structure (Figure 2.1), consisting of two leads A and B separated by a very thin barrier C of a non-superconducting material, generally called a *weak link*. Such a structure is an example of a *junction* [22, 23] but other geometries are also possible.

Depending on the materials chosen for A, B and C one can distinguish several relevant junctions, for example NIS, SIS, SNS, S-TI-S and N-TI-S junctions. Here N stands for 'normal metal', I stands for 'insulator', S stands for 'superconductor' and TI stands for 'topological insulator'. The latter junctions are subject of the present thesis. It is assumed that junctions are studied below the critical temperature of the superconductor.

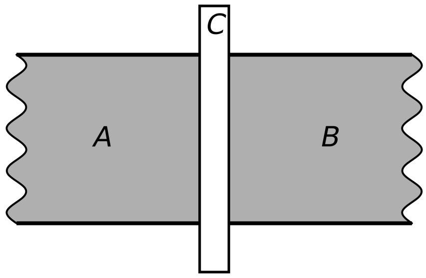

Figure 2.1: Junction configuration, A and B are either a superconducting material or a normal metal whereas C is not and very thin. Figure from Miraceti, commons.wikimedia.org.

Ordinary electron (quasiparticle) tunnelling can take place as long as there are empty states above the Fermi level or superconductor band gap, on the other side of the barrier, to tunnel to. An applied potential difference over the junction aids this process by giving the electrons sufficient energy to overcome the superconducting gap of the superconductor. This gives always rise to a resistance. In the SNS, S-TI-S and N-TI-S, one cannot speak of tunnelling, since transport can take place via the normal metal barrier. Only at the interface between the superconductors and the barrier material there might be an additional interface barrier. Cooper pairs may also be involved in the normal particle transport due to Andreev reflection, giving rise to sub-gap transport; this will be discussed in a separate section.

When the junction consists of two superconducting leads (SNS, SIS and S-TI-S junctions), also Cooper pairs can tunnel in the superconducting regime. This gives rise to a supercurrent at zero applied voltage, this is called a *DC Josephson supercurrent*, which is the topic of the next section. Junctions showing a Josephson current are called *Josephson junctions*.

The DC Josephson supercurrent results from the phase difference $\gamma = \phi_A - \phi_B$ of the macroscopic wave function of the superconducting leads on either side of the junction (or barrier):

$$I = I_0 \sin\gamma \tag{2.1}$$

At zero applied voltage a current can be forced trough the junction with a maximum current of I_0, above this value the junction becomes resistive and a voltage appears. The maximum Josephson current I_0 is usually related to the superconducting gap Δ, both are temperature dependent. A typical I,V-curve is shown in Figure 2.2(a).

Fraunhofer I_c modulation

The Josephson supercurrent I oscillates in the presence of a varying magnetic flux ϕ_B according to the following sinc-function:

$$I = I_0 \frac{\sin\left(\pi\phi_B/\alpha\phi_0\right)}{\pi\phi_B/\alpha\phi_0} = I_0 \operatorname{sinc}\left(\frac{\pi\phi_B}{\alpha\phi_0}\right) \tag{2.2}$$

In this equation ϕ_0 is the magnetic flux quantum, a constant defined by $\phi_0 = \frac{h}{2e} \approx 2.0678 \cdot 10^{-15}$ Wb, I_0 is the (critical) current at zero field, which depends on the temperature during the measurement (Eq. 2.1). The magnetic flux is related to the magnetic field by $\phi_B = B \cdot A$, for magnetic fields B perpendicular to the area A of the junction (in general cases: $\phi_B = \iint \vec{B} \cdot \mathrm{d}\vec{a}$). The constant defined by α can be either one or two: one for a normal material in the gap and two for a topological protected material in the gap [15]. This graph of the sinc-function is referred to as the *Fraunhofer pattern* because of its shape resemblance with the optical phenomena of Fraunhofer diffraction, an ideal Fraunhofer diagram is shown in Figure 2.2(b).

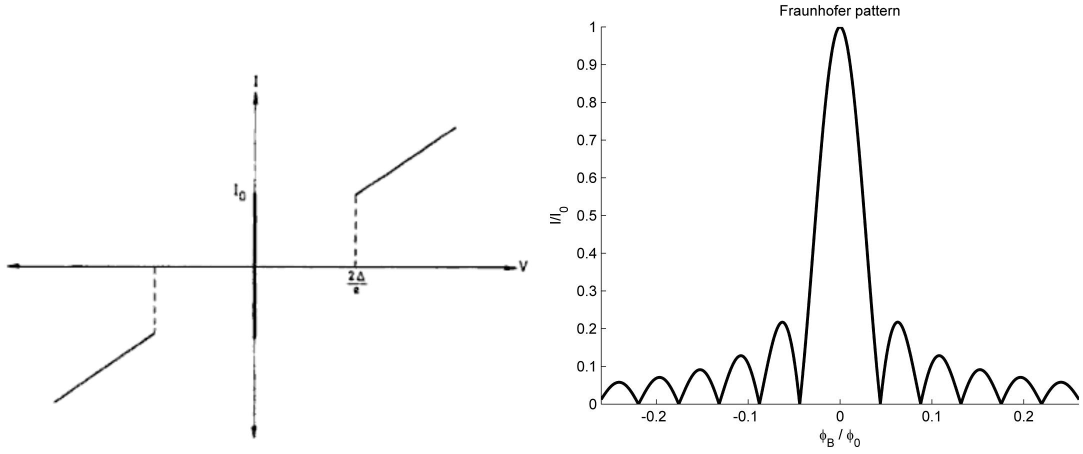

(a) (b)

Figure 2.2: (a) An ideal current-voltage graph of a Josephson junction at $T = 0$ K, image from [22]. At zero voltage a DC Josephson current is observed. Voltages corresponding with energies below the gap give only rise to a current for $T > 0$, due to thermally excited electrons. Voltages above the energy gap ($V > 2\Delta/e$) give rise to resistive normal electron transport or tunneling. (b) An ideal Fraunhofer pattern for a junction with a junction area of 0.03 μm^2 and $\alpha = 2$ (topological protected material in the gap).

The above equation for the magnetic field dependence Josephson tunneling current, Eq. 2.2, holds strictly only in the limit of an infinitely wide junction and a homogeneous current density distribution [15]. Any deviation from this ideal situation will lead to deviations in the Fraunhofer pattern. Practically, this will always happen, because the junction width will be finite. This makes it non-trivial to analyze the Fraunhofer pattern [15].

2.1.2 The BTK-formalism

Blonder, Tinkham and Klapwijk (BTK) published in 1982 [24] a theory, know as the BTK-theory, that describes the transmission and reflection of particles at a normal metal-superconductor (NS) interface as a function of the barrier strength Z, from which the corresponding I,V-curves can be calculated.

From an analysis based on the Bogoliubov equations and a generalized semiconductor model, they identified the transmission and reflection coefficients of three single quasiparticle (electron or hole) processes – two transmission processes and one reflection process – and one pair process. The latter is called Andreev reflection and can, in contrast to the quasiparticle processes, also take place at energies less than the superconducting gap: $|E| < \Delta$. The transmission and reflection coefficients they calculated for each process and arbitrary barrier strength Z, can be found in Table II of their publication [24]. From this they calculated the differential conductance for various barrier strength, as shown in Figure 2.3(b). In these plots the conductance is maximal at the superconducting gap Δ, when a barrier is present.

Whereas the BTK theory deals with conventional (s-wave) superconductivity, the tunnelling conductance of unconventional superconductors have also been calculated, for example by Eschrig and colleagues [25]. This will be referred to as 'adapted BTK-formalism'.Here chiral p-wave ($p_x + ip_y$) superconductivity is the most interesting, since this is the superconductivity that can be induced in the surface states of a topological insulator [3]. The term chiral refers to the fact that the motion of the electrons in the surface state is only in one direction [4]. More details on topological insulators will be discussed in a later section.

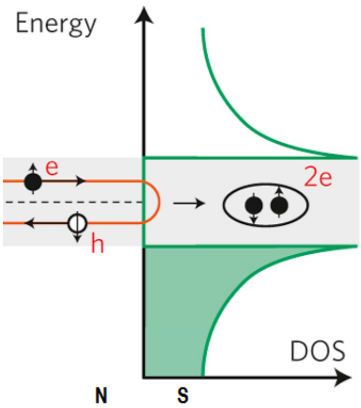

(a)

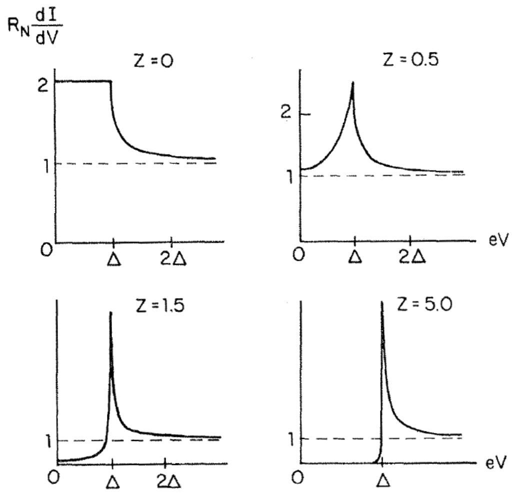

(b)

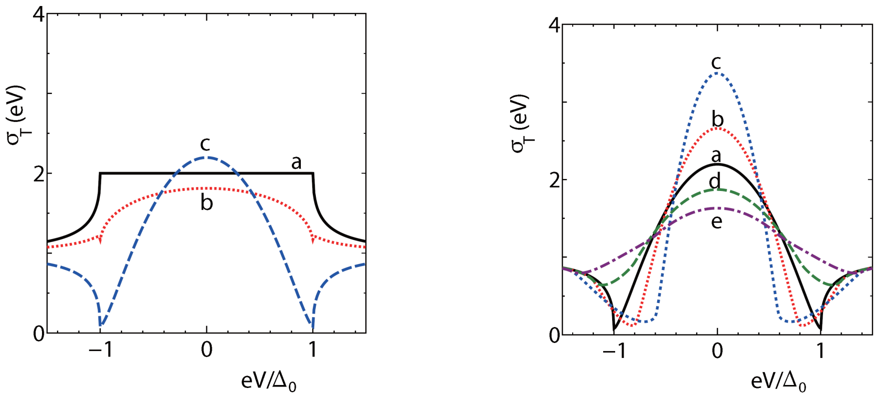

(c)

Figure 2.3: (a) Graphical display of Andreev reflection at an NS interface. An electron can enter a superconductor at energy $\epsilon = E - E_F$ by pairing with an electron from $-\epsilon$ with opposite momentum and spin, to form a Cooper pair and thus reflecting a hole at energy $-\epsilon$. (Image after [29]). (b) Simulation of the differential conductance vs. voltage for various barrier strengths Z at $T = 0$, from the BTK theory for s-wave NS interfaces. (Graphs from [24]). (b) Simulation of the tunnelling conductance of a chiral p-wave NS interface. In the left figure the letters indicate the following situations in zero perpendicular magnetic field (i.e. $H = 0$); a: $Z = 0$, b: $Z = 1$ and c: $Z = 5$. In the right figure the letters indicate the following situations in the absence of a barrier (i.e. $Z = 0$); a: $H = 0$, b: $H = 0.2H_0$, c: $H = 0.4H_0$, d: $H = -0.2H_0$ and e: $H = -0.4H_0$. (Graphs from [25]).

Calculated graphs of this system are shown in Figure 2.3(c) for several situations. In these plots around the superconducting gap Δ the conductance is minimal in the non-trivial case.

In both the s- and p-wave NS contacts conductivity is possible inside the gap. In the case of p-wave superconductivity this is observed as a broad peak, see Figure 2.3(c). This is due to Andreev reflection, which makes it possible to transport Cooper pairs around the Fermi level (zero energy, if viewed relatively to the Fermi energy). Andreev reflection will be discussed in the next section.

2.1.3 Andreev reflection, (Andreev) Bound State and Majorana fermions

At the interface between a normal metal and a superconductor, single electrons can be transferred from the metal to superconductor only when its energy is larger than the energy gap of the superconductor ($E > \Delta$). Inside the gap transport of electrons is only possible if an electron finds an electron partner to enter the superconductor as a Cooper pair. This involves the retroreflection of a hole with opposite spin and (nearly opposite) momentum into the metal, to fulfill the conservation laws. The partner electron has opposite momentum and spin compared to the first electron and is extracted from the metal at an energy just as much below the Fermi level as the first electron was above. This process is called Andreev reflection [27] and is graphically shown in Figure 2.3(a). In ideal Andreev reflection, i.e. in the absence of a barrier ($Z = 0$) as mentioned in the BTK theory, the conductance is twice as large as single electron conductance in the normal state, since two electrons are involved. When a barrier ($Z \neq 0$) is present, the Andreev reflection is suppressed or destroyed for s-wave superconductivity, see Figure 2.3(b), or changes its energy distribution in p-wave superconductivity, see Figure 2.3(c).

In a SNS contact effectively two NS junctions exist. This leads to Andreev bound states. An electron in a normal metal moving to the right, can at the NS interface be converted in a retroreflected hole and a Cooper pair in the right superconductor. The retroreflected hole will now move to the left NS interface, where it can be backconverted in an electron and break up a Cooper pair in the left superconductor. If this electron returns to its starting position with the same phase and keeps reflecting, a bound state is formed and Cooper pairs are transported through the normal metal, i.e. a supercurrent flows. A state will only exist when the electron returns to its initial position with the same phase, after one cycle. This will result in quantized energy levels for the bound states (due to the wave nature of electrons), that depend on the phase difference of the wave functions of the superconductors.

Andreev reflection can also cause bound states in NS contacts itself, aided by normal particle reflection at the interface of the (thin) normal metal with the vacuum. This method was used by Mourik and colleagues [28] to find indications of Majorana fermions in a p-wave induced semiconductor nanowire.

For p-wave superconductivity, bound states can be observed as a broad Zero Bias Conductance Peak (ZBCP) in the differential conductivity of the NS junction, see Figure 2.3(c). It can be seen that this ZBCP grows with an increasing magnetic field. If the normal metal is a p-wave induced topological insulator (or p-wave superconductor) an extra ZBCP from a zero energy state (relative to the Fermi level $E - E_F$) might be found. Since one expects Majorana fermions at zero energy, the appearance of such a ZBCP could be an indication of the presence of a Majorana fermion (see Section 2.3.1).

In theory a zero-energy Andreev bound state is also possible for NS contacts, but since always a finite interface barrier is present this is in practice not realizable. Particles in the normal metal at zero-energy will not have enough energy to overcome this barrier and reflect. Therefore, Andreev reflection and consequently a Andreev bound states, are not possible at zero energy. In a topological insulator perpendicular reflection is prohibited because particles picks up a π-Berry phase. For other angles of incidence the Berry phase does not equal π, and reflection (backscattering) is possible [30]. This argument will become clear in a moment when topological insulators are discussed in Section 2.2.1. Therefore zero-energy (Majorana) bound states are possible in N-TI-S junctions.

2.1.4 Proximity effect

A superconductor in close contact with a normal metal shows a *proximity effect* [22]. Due to the overlap of wave functions at the interface some Cooper pairs 'leak' into the normal metal, while some quasiparticles from the normal metal 'leak' into the superconductor. Superconductivity is induced in the metal over a distance called the normal coherence length ξ_n, the value depends on the amount of disorder in the normal metal, as indicated by the electron mean free path in the metal l_e. Two regimes can be identified:

$$\text{'clean limit' } (\xi_0 \ll l_e,)\text{: } \xi_n = \frac{\hbar v_F}{k_B T}, \tag{2.3}$$

$$\text{'dirty limit' } (\xi_0 \gg l_e)\text{: } \xi_n = \sqrt{\frac{\hbar v_F l_e}{6\pi k_B T}}, \tag{2.4}$$

where ξ_0 is the coherence length of the superconductor and v_F is the Fermi velocity in the metal.

2.2 Topological insulators

Topology is the mathematical study of the properties that are preserved through deformations, twistings and stretchings of objects, conversely tearing (and then gluing) is not allowed [31]. With this definition in mind it will become clear below why the word 'topological' is used in the physics described here.

Topological insulators are materials with an insulating bulk but at its surface it is necessarily conducting due to its topological nature. One can imagine that a lot of interesting physics is behind this, only a small and basic part will be discussed below, the reader is referred to the reviews of Qi and Zhang [2] and Hasan and Kane [4] for an extensive discussion.

2.2.1 A quantum spin Hall state

The 'normal' Quantum Hall Effect (QHE) occurs when a strong magnetic field is applied over a 2D electron gas in a semiconductor, at low temperatures. The magnetic field causes the electrons to confine in circular orbits, at the edge the orbits cannot be closed and thus only at the edges conducting channels are formed. So, only at the upper and lower edge channels exist where electrons will move in opposite directions, in between there are no channels and is thus insulating, this is sketched in Figure 2.2.1(a). Since the two channels are spatially separated, dissipation (scattering) is impossible since the spatial overlap of the wave functions is reduced [32]; carriers will simply move around the scatters [14].

A 2D topological insulator is a quantum spin Hall (QSH) state. The latter is closely related to the QH state, but now the spin degeneracy is lifted, see Figure 2.2.1(b). In a 2D topological insulator this is realized by a strong spin-orbit coupling, even in the absence of a magnetic field. At both edges spatially separated conducting states appear of both opposite spin and momentum. This system is time reversal invariant and backscattering from a non-magnetic impurity is impossible. Just like in the QH effect it is impossible to scatter to a state on the other side of the sample, but it is also impossible to scatter to another spin state on the same side. Figure 2.2.1(c) makes this clear. An electron can reflect in two ways around a non-magnetic impurity, either clockwise or counter clockwise, where the spin rotates by an angle of π or $-\pi$ respectively. This gives a phase difference of 2π between the time reversed

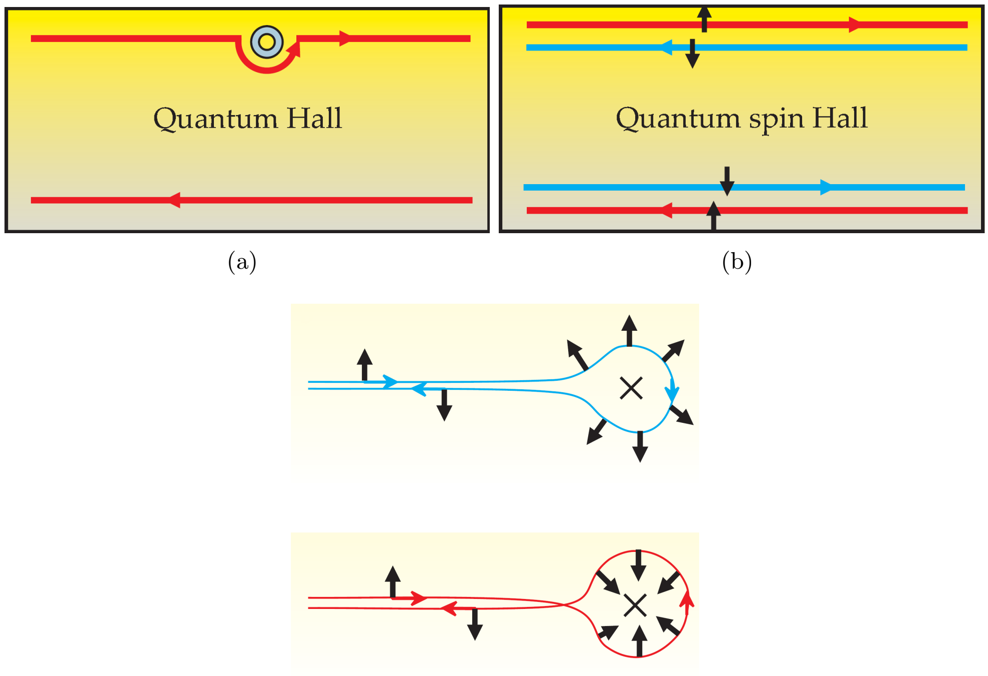

(a) (b)

(c)

Figure 2.4: Graphical depiction of the QH effect (a), the QSH effect (b) and reflection on a non-magnetic impurity in a QSH sate. Figure from [14].

paths. This results in a geometric Berry phase of $2\pi/2$ and, hence, a negative sign of the wave function of a spin-1/2 particle and therefore they interfere destructively [14, 2]. On the other hand, scattering on a magnetic impurity will result in a spin flip and time reversal symmetry is broken.

Although all the previous was described for a 2D case, it can be generalized to a 3D situation, where the edge states will become surface states [4]. The question that remains is how the spin-orbit coupling gives rise to these edge or surface states, this follows from the topological band theory, which will be discussed next.

2.2.2 Topological band theory and 3D topological insulators

In topological band theory, the order of the energy bands determines the difference between a normal insulator phase and a topological insulator phase. As an example of a 3D TI we take Bi_2Se_3, other known 3D TI are for example Bi_2Te_3 and BSTS, these are all layered materials comparable with the structure of BSTS and CBS, as discussed in the introduction. The bands of Bi_2Se_3 closest to the Fermi energy and at the Γ symmetry point of the Brillouin zone, are shown in Figure 2.2.2. Zhang and co-workers [33] explained how these orbitals lead to the formation of a band inversion at the Fermi energy. They consider three stages (as indicated in the figure) going from the atomic p-orbitals of Bi and Se to the conduction and valence bands of Bi_2Se_3. The first step (I) involves the bonding and hybridization of Bi and Se orbitals, then crystal-field splitting is accounted for in stage (II) and finally in stage (III) spin-orbit coupling lifts the degeneracy of the bands and pushes one band up and the other down. This makes that two bands cross near the Fermi energy (second green box in the Figure) if the spin-orbit coupling is strong enough to push the bands far enough up and down. The valence band has become a conduction band and vice versa.

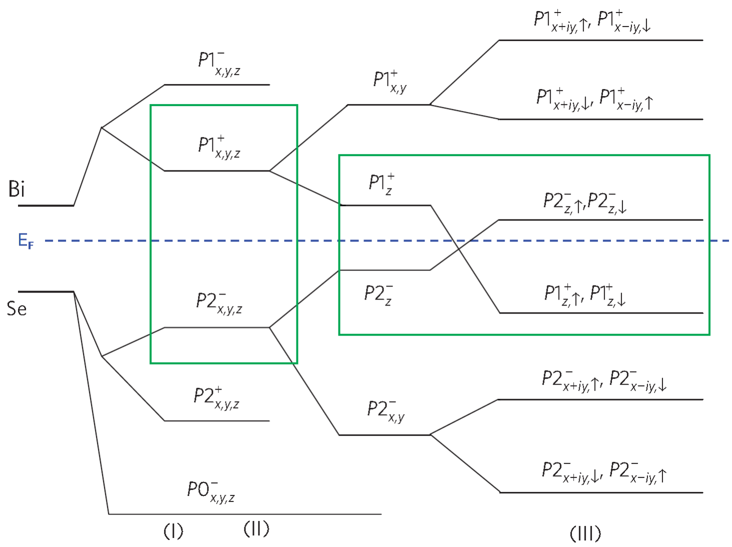

Figure 2.5: A schematic diagram showing how the p-orbitals of Bi and Se around the Fermi energy (blue line) at the Γ-point, result in a crossing of a band of Se and Bi trough the bandgap. Figure from [33].

In a topologically trivial insulator, vacuum or a normal insulator, the bands are not inverted. Therefore, at the interface of a TI with a topological trivial insulator the conduction and valence bands have to change position again. Therefore the bands always have to cross the band gap at the interface of two topological different materials, which dictates the existence of a metallic surface state. In the vicinity of the crossing point the dispersion of the states is approximately linear. Here particles are 'massless' and can be described by the Dirac equation. In three dimensions this linear crossing forms a Dirac cone.

2.3 Superconductors and TI: quasiparticle Majorana fermions

2.3.1 Majorana fermions

In 1937 Ettore Majorana introduced the concept that is now know as the 'Majorana fermion': a particle that is its own antiparticle, or in the language of quantum mechanics:

$$\gamma = \gamma^{\dagger}, \tag{2.5}$$

Normally particles and antiparticles can annihilate, thereby producing a pair of photons [34]. A fermionic particle with the exceptional property of Eq. 2.5 has not been (fully) detected up to now.

In solid state systems, Majorana fermions are not fundamental particles, but are special combinations of ordinary electrons and holes [35]. The main systems where condensed matter physicists are looking for Majorana fermions are *Topological Insulator - Superconductor interfaces* and *Topological Superconductors*. In the past years some 'signatures' have been found [28], but it turns out to be hard to unambiguously show the existence of a Majorana fermion in solid state systems.

Superconductors are an obvious first place to look for Majorana fermions since their quasiparticle operators consists of superpositions of electrons and holes [35]. Normally this consists of an electron at energy level $+E$ and a hole at energy level $-E$. Only at the Fermi level (E=0), which is in the middle of the superconducting gap, the eigenstates are charge neutral superpositions of electrons and holes [34]. Obviously, also the creation an annihilation operators for an excitation at energy E are then equal [34]:

$$\gamma(E) = \gamma^\dagger(-E) \tag{2.6}$$

Which is a general symmetry for superconductors.

The conventional superconductivity is s-wave superconductivity, where Cooper pairs have opposite spin projections. On the other hand, p-wave superconductivity has equal spin projections. The fact that the spins are equal in p-wave superconductivity results in equal quasiparticle creation and annihilation operators (e.g. $\gamma = uc_\sigma^\dagger + u^* c_\sigma$, with σ the spin projections), a defining property of the Majorana fermion [5]. So Eq. 2.6 holds only for p-wave pairing.

This brings us to the second requirement: the superconductors need also to be 'spinless' [35]. Because the spins of the fermions in such a system are equal, one speaks of a 'spinless' system. This makes s-wave superconductors in proximity to a topological insulator a likely candidate, because p-wave superconductivity can be induced in the surface states of a topological insulator by the proximity effect, since the surface states are not spin degenerate but contain only particles with one spin projection [4].

By inducing superconductivity a gap is opened in the surface states around the Fermi level, but at the interface with a normal part of the TI, local subgap states can arise [34]. At this point the sought after zero energy levels for Majorana fermions arises. Therefore Majorana fermions can bound at (normal cored) vortices induced by a magnetic field, in this particular case the boundary conditions on the wave function dictates a flux of $hc/2e$ in order to have a zero energy mode, i.e. Majoranas [35]. Since an applied magnetic field breaks time reversal symmetry only one Majorana mode will exist at the vortex.

Besides this, Fu and Kane [3] proposed that Majorana fermions would appear at the edge of the superconductor-topological insulator crossing of a S-TI-S junction, only if the phase difference between the superconductors is equal to π and the momentum has no component parallel to the junctions width. Then a zero energy Andreev bound state exists in the junction giving rise to two (on each edge of the junction) nonchiral "Majorana quantum wires" along the width of the junction [36].

Interestingly, it is proposed that there also exist superconductors with surface states as in topological insulators, these materials are called topological superconductors. The expected topological insulator $Cu_xBi_2Se_3$, has already been discussed in the introduction. For these materials the superconductivity is inherent, and does not have to be induced by the proximity effect.

2.3.2 How to detect a Majorana fermions in S-TI junctions?

Several ways to detect a Majorana fermion have been proposed [34], here we restrict the discussion to two important mechanisms for detecting a Majorana fermion in a S-TI junction. The first option is through the observation of a zero bias conductance peak in N-TI-S tunnel junctions, which has already been discussed. As a second option, an indication of the presence of a Majorana fermion in a pS-TI-pS Josephson junction can be found by studying the Josephson supercurrent of the junction. Usually only Cooper pairs (charge $2e$) tunnel in the Josephson effect, but the Majorana fermions enable the possibility of single electron (charge e) tunneling with a larger probability [34]. This doubles the usual 2π periodicity in the superconducting phase difference of the Josephson supercurrent. This is called the fractional Josephson effect [37]. The AC Josephson effect will give rise to Shapiro voltage steps with a doubled step height [38], but only for perpendicular channels (see [30] for a discussion).

2.4 Quantum corrections to resistivity and conductivity

Normally, resistance decreases with temperature. But there exist corrections to the low temperature regime due to the wave nature of electrons; the corrections are collectively called the 'quantum corrections to resistivity/conductivity'. They exist due to electrons scattering from violations of the periodicity of the lattice, e.g. defects, impurities etc. Two effects commonly observed in Bi-based topological insulators are weak antilocalization (WAL) and electron-electron interactions (EEI), both will be discussed in this section.

2.4.1 Weak (anti)localization

Weak (anti)localization [40] is a correction that results due to electron waves interference with itself after several scattering events of partial waves along a diffusive closed path. This will only occur as long as the electron wave returns to its starting position before the particle forgets its initial phase. This defines the phase breaking time τ_ϕ, the distance an electron can travel in this time by diffusion is defined as the phase breaking length L_ϕ, or dephasing length. At the initial position the electron waves of different paths, that return to the initial point, interfere. This leads to an upturn in resistance for the lowest temperatures in the case of weak localization (WL), due to constructive interference, since the electron has a higher probability to be found at the initial point, staying more localized. Therefore WL is also referred to as 'enhanced backscattering'. In the case of weak antilocalization (WAL) destructive interference takes place and the resistance is decreased, since there is less change for an electron to stay localized.

Weak antilocalization is commonly observed in Bi-based 3D TI [15]. Here WAL can be caused by strong spin-orbit coupling in the bulk and spin-momentum locking in the surface states [42]. The latter can be explained by the π Berry phase which prohibits backscattering from non-magnetic impurities, as discussed in Section 2.2.1, which at the same time excludes the appearance of WL in surface states of TIs as long as time reversal symmetry is not broken [15]. In fact, from this same argument it follows that electrons cannot be localized, no matter how strong the disorder [4]. In the bulk, WAL arises from a spin flip during scattering in the presence of spin-orbit coupling. Now it may interfere destructively with the coexisting wave with the same spin projection [40].

Weak antilocalization is reduced or destroyed by a magnetic field. An electron wave acquires an extra phase factor when travelling along a loop in a magnetic field. Electron waves in the loop travelling in different directions acquire a phase difference that can destroy the interference. The dependence of the 2D (surface state) correction to the conductivity due to W(A)L in a perpendicular magnetic field is given by the Hikami-Larkin-Nagaoka (HLN) equation [43]:

$$\begin{aligned}\Delta\sigma(B_\perp) &= \sigma(B_\perp) - \sigma(0) \\ &= \alpha\frac{e^2}{\pi h}\left[\Psi\left(\frac{1}{2} + \frac{\hbar}{4eL_\phi^2 B_\perp}\right) - \ln\left(\frac{\hbar}{4eL_\phi^2 B_\perp}\right)\right],\end{aligned} \tag{2.7}$$

where Ψ is the digamma function. For WL $\alpha = 1$ and for WAL in Bi-based TI $\alpha = -0.5$, or -1 if you account for both the top and bottom surface states of the TI.

The phase breaking length L_ϕ depends on temperature, therefore the correction to conductivity is also temperature dependent. In the absence of a magnetic field the following relations hold for two dimensions [44, 45]:

$$\Delta\sigma_{W(A)L,2D}(T, B = 0) = \frac{e^2}{\pi h}\alpha p \ln\left(\frac{T}{T_0}\right), \tag{2.8}$$

and for 3D (bulk):

$$\Delta\sigma_{W(A)L,3D} \propto T^{-p/2}. \tag{2.9}$$

Here, p is a constant that depends on the source of the inelastic scattering, and T_0 is the reference temperature from which the deviation $\Delta\sigma$ is measured [45]. A plot with a logarithmic temperature axis will directly show the functional dependence and thus if the 2D or 3D relation applies.

2.4.2 Electron-electron interactions

Electrons can also interfere with each other (instead of with themselves as in W(A)L), which can give rise to electron-electron interactions (EEI) [40]. If two electrons have the same initial phase at a certain point, there is a change that they meet again and interfere within the dephasing time τ_{ee}. For electron-electron interactions this effective time of the interaction $\tau_{ee} = \hbar/(E - E_F)$ is larger near the Fermi energy, this effects the exchange interaction in the Hamiltonian (and thus the energy levels) [40, 41]. The result is that energy levels around the Fermi level are pushed away, therefore a minimum in the density of states at the Fermi energy (E_F) is then observed.

The correction to the 2D conductivity due to EEI is given by:

$$\Delta\sigma_{EEI,2D}(T) = \frac{e^2}{2\pi h}\left(2 - \frac{3}{2}\tilde{F}\right)\ln\left(\frac{T}{T_0}\right), \tag{2.10}$$

where $\tilde{F}$ is a Coulomb screening factor with a value between zero and unity [46]. Again, for 3D the correction involves a square root dependence on temperature, the exact equation is given in [44].

In the presence of a magnetic field, Zeeman splitting will introduce a further correction to the conductivity [45, 44, 47]:

$$\Delta\sigma_{EEI,2D}(B) \approx -\frac{e^2}{2\pi h}\tilde{F}\ln\left(\frac{g\mu_B B}{1.3\mu_0 k_B T}\right). \tag{2.11}$$

This approximations holds as long as $g\mu_B B/\mu_0 k_B T \gg 1$, i.e. the Zeeman splitting is much larger than thermal activation. Here, g is the Zeeman g-factor (for the surface states of BSTS $g \approx 20$ [11]), $\mu_0 = 4\pi\cdot 10^{-7}$ Vs/Am is the permeability of free space and $\mu_B \approx 9.274\cdot 10^{-24}$ J/T is a constant called the Bohr magneton.

Unlike WAL, this correction is isotropic to magnetic field, thus measurements in parallel and perpendicular fields could indicate whether WAL, EEI or both contribute to the correction, as was done by Liu and colleagues [47].

Since the functional dependence of the WAL and EEI corrections to conductivity are the same it is difficult to distinguish between these effects in transport measurements. Tunnelling experiments, on the other hand, show the minimum in density of states indicative of EEI [40].

Chapter 3

Manufacturing junctions on topological insulators

Working with BSTS and CuBiSe topological insulators is quite challenging. This is mainly due to the fact that no thin films were available for this project. It was only possible to use crystals grown by a modified Bridgman method [12, 11, 16] for BSTS or in our case for CuBiSe by a method described in [18] Both crystals were provided by the the 'Quantum Electron Matter' group of the University of Amsterdam.

In order to transfer the topological insulators to the substrate, we used the process of 'micro-mechanical exfoliation', more appropriately called the 'Scotch-tape' method. This results in small flakes of the order of ten to hundred quintuple layers thick and a lateral size in the order of 10 µm. Furthermore, leads and Josephson junctions for the measurements are deposited on the flakes by photo- and electron beam lithography and sputtering techniques. The details of device manufacturing will be discussed in more detail in this chapter.

3.1 Sample preparation

All the samples were prepared on a substrate of SiO_2/Si (with either 100 nm (Si p^{++} doped), 300 nm (Si p^{++} doped), 1 µm or 6 µm SiO_2 (Si p-type doped)). Before depositing flakes, the substrates are ultrasonically cleaned in acetone and afterwards washed with acetone and ethanol, and dried with nitrogen.

The topological insulator crystals are kept at high vacuum, because in particular BSTS is very sensitive to air exposure, resulting in n-type doping of the surface of BSTS when exposed to air. This effect causes a time evolution of the transport properties of BSTS, after cleaving [11].

The flakes are deposited outside the vacuum chamber by a technique called micro-mechanical exfoliation. A thin layer of the topological insulator is cleaved from the crystal with Scotch tape. This thin layer is further reduced to a few (order ten to hundred) quintuple layers by multiple cleavings with Scotch tape. Next, the layer is transfered to the substrate by pressing the tape on the sample and brushing it with force. When the tape is peeled off, small flakes of the topological insulator material stick to the surface by Van der Waals or electrostatic forces [7]. The flakes are loosely bound by these forces and can easily be wiped off the substrate, which makes working with flakes quite challenging.

On each sample a flake that fulfills the criteria of large size, smooth surface and small thickness, is selected to be used for further processing. In practice this selection is done at the mask aligner during the lithography procedure, because not every flake selected under a normal optical microscope is visible with the mask aligner. The minimal size of a flake is determined by the size of the lithography mask, therefore the flake should be at least 14 µm by 23 µm. Most flakes are smaller than this size, good flakes are rarely much larger than this. Images of the lithography mask and the resulting leads on a CuBiSe flake are shown in Figure 3.2(a) and 3.2(b), respectively.

An example of a typical BSTS flake is shown in the AFM scan of Figure 3.1. One can clearly see the layered structure of a flake and the relatively flat plateaus. The thickness of a typical flake is of the order of 100 nm (in this case between 80 nm and 200 nm). The flake shown here is too small to deposit leads on.

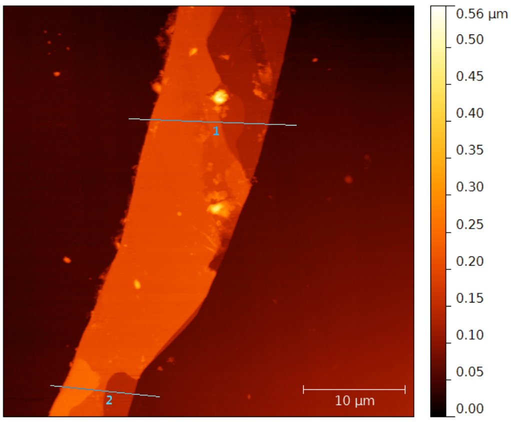

(a)

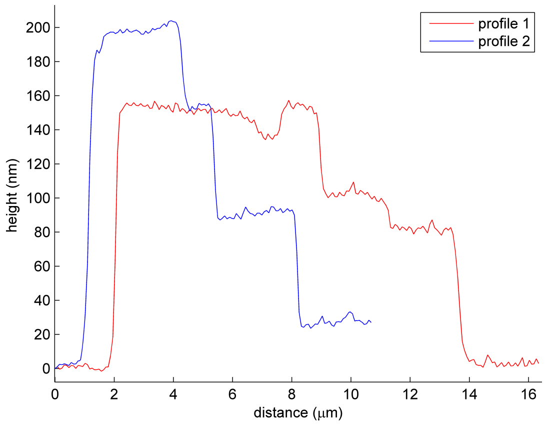

(b)

Figure 3.1: (a) An AFM scan of a flake on sample 49 (b) Height profiles of the flake across the profile lines as indicated in (a).

It is important that the flakes used for Josephson junctions have a smooth surface in order to minimize unknown and undesired effects of steps and roughness. Furthermore, flakes need to be thin, so the leads and the junction do not have to be very thick – there is a limit on the thickness of the photoresists that can be used for both normal as e-beam lithography. Thinner flakes have also less bulk, which results in less less bulk contribution in our measurements [13]. Generally the quality of a flake can be judged fairly well under an optical microscope, thick flakes show dark boundaries, while rough flakes show islands, steps or appear darker in color due to scattering. Normal flakes are bright and white, but really thin flakes – generally only realized after etching – appear blue, the lighter blue, the thinner the flakes. In practice it is difficult to work with these flakes because they are not visible in the mask aligner.

3.2 Optimizing lithography, sputtering and lift-off

In order to deposit leads and Josephson junctions on the flakes, a suitable manufacturing procedure had to be found. In principle this process consists of the following steps:

1. Spinning a suitable photoresist (photolithography);
2. Positive or image reversal UV exposure procedure (photolithography);
3. Developing the photoresist (photolithography);
4. Sputtering Nb(/Pd) or Au;
5. Lift-off of the sputtered materials;

In case of the manufacturing of Josephson junctions the process continues:

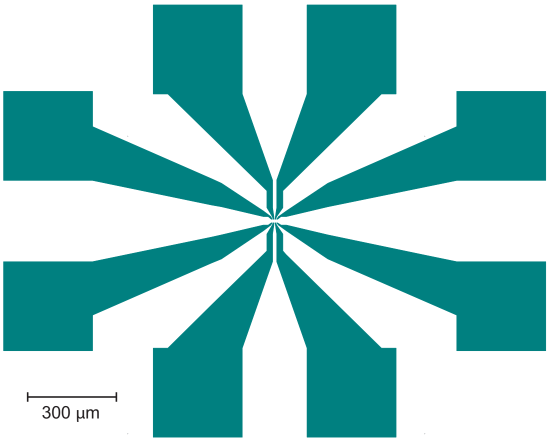

(a)

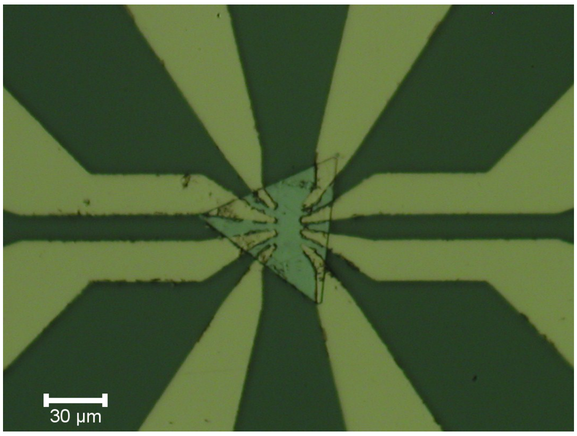

(b)

Figure 3.2: (a) The photolithography mask used for making niobium or gold leads to a flake. (b) Gold leads deposited on a unique triangular CuBiSe flake.

6. Preparing the samples for e-beam lithography (removing ears and spinning PMMA etc.);
7. E-beam lithography;
8. Sputtering Nb or Au;
9. Lift-off of the sputtered materials;

Starting from a procedure that has been used before for Bi_2Te_3 flakes, both the manufacturing procedures of BSTS and CuBiSe devices were optimized. This will be discussed below in separate sections for the different devices.

3.2.1 Niobium Josephson junctions on BSTS

Josephson junctions with niobium electrodes were made on BSTS for the measurements discussed in the next chapters. Niobium was chosen for the leads because it is a well-studied superconductor with a reasonable high critical temperature (9.2 K, [22]) and coherence length (38 nm, [22]), which can be easily deposited by standard sputtering techniques.

In the first step 200 nm thick niobium leads were deposited by DC sputtering[1] on a suitable flake following the procedure sketched above. In the first and fifth step of this procedure, either a positive or an image reversal photoresist can be used. Lift-off with image reversal photoresist goes slightly better, but it takes much longer time to process because of the additional steps in the photolithography (see both optimal positive and image reversal recipes in Appendix A). This is due to the fact that the image reversal photoresist was more than two times thicker and has a small undercut.

Acetone is used as a solvent for the photoresist, followed by an acetone and ethanol flush, to remove the niobium remainders. Both resists give large ears to the structures after lift-off, but ears of samples with image reversal photoresist can be removed more easily afterwards. This was realized by softly sliding the sample over a acetone drenched (lens) tissue. Therefore the image reversal photoresist is preferable. Ears on the leads must be removed in order to get a good contact with the Josephson junctions deposited in the next steps, Figure 3.4 makes this clear.

[1] All (optimized) deposition schemes can be found in Appendix B.

In SEM images after positive resist lithography it appeared that large ears only existed at positions where the niobium leads touched the BSTS, this can be seen clearly in Figure 3.4. Therefore it was suggested that those ears resulted from reflections of the UV-light on the BSTS during exposure.

In one of the first measurements it turned out that it was not possible to measure a supercurrent through two connected niobium leads, it was proposed that this is due to the oxidation of the niobium top layer. In order to overcome this problem in the next samples, a thin layer of 2.3 to 5 nm palladium was deposited directly after the deposition of niobium, without removing the sample form the vacuum chamber. Palladium does, in contrast to niobium, not oxidize at reasonable temperatures. As long as the layer of palladium is thin enough (a few nanometers) it will not influence the superconductivity because of the proximity effect. The layer of palladium between the leads and the e-beam structure will be even thinner than the deposited amount, due to substrate cleaning before depositing the last layer of niobium.

E-beam lithography

After the leads are deposited, an e-beam step follows in which the junctions are written in a PMMA resist, which is spin coated on the samples. The pattern written in the PMMA, with the junctions of the measured samples, is shown in Figure 3.3. The pattern is made to overlap the niobium leads for obvious reasons. Parameters of the e-beam had to be optimized such that junctions have the correct size and are not under- or overexposed[2]: 10 kV acceleration voltage, 10 µm aperture, a working distance of 10 mm and a dose of about 140 $\mu C/cm^2$. The exact dose turned out to be different for every flake. After the writing the PMMA is developed in a MIBK:IPA (1:3) solution and a IPA stopper, next 30 to 80 nm of niobium was sputtered on top (depending on the thickness of the used PMMA resist).

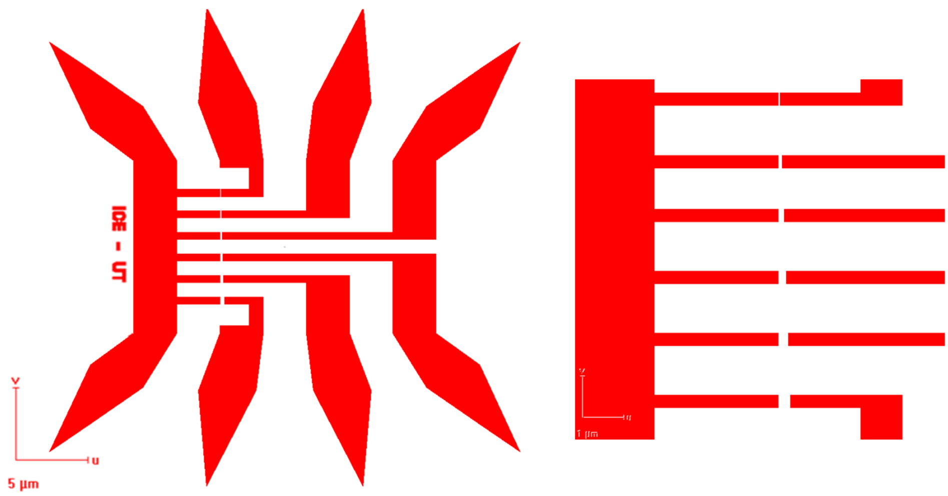

Figure 3.3: The e-beam pattern used in the measured samples. The pattern defines five Josephson junctions with a junction width of 300 nm and junction lengths ranging from 50 to 300 nm. The left images shows a full overview of the structure, whereas the right image shows a zoom on the junctions.

A quite challenging lift-off procedure in acetone and subsequently flushing with acetone and ethanol follows. Initially it was difficult to remove the niobium from undesired positions. In the way to successful lift-off, several things were tried: long time in acetone (up to 36

[2]The reader is referred to the last section of this chapter for a note regarding these settings.

hours), (short) ultrasonic bath cleaning (in double beakers), removing remainders with a swab, lift-off in heated acetone ($T < 55°$C), Scotch tape (which quite obviously did not work) and softly sliding the sample over a acetone drenched (lens) tissue. None of these proposed solutions resulted in sufficient lift-off without damaging the flake or the junctions, only the (lens) tissue method and a short ultrasonic cleaning (3 seconds) led to some improvement. Lift-off also improved when the number of junctions on a flake was reduced, the junction width was made smaller (from 500 to 300 nm) to increase the separation between junctions and when less niobium was deposited (30 nm instead of 80 nm on PMMA A2 resist). In the end the solution for a good lift-off was found in increasing the PMMA thickness to 298 nm – and thus getting a better ratio between the PMMA and the niobium thickness, while having thick enough niobium to be superconducting, to contact to the leads and to overcome steps in the flake. This was realized by using the thicker PMMA A4 resist instead of the PMMA A2 resist, while keeping the subsequent deposition of niobium on 80 nm. It has to be noted that by using a thicker PPMA one has to compromise on the resolution one can reach with the e-beam. Afters some tests, we considered the resolution to be good enough for a set of initial junctions (see Figure 3.3) to test whether or not a supercurrent could be measured. A further reduction of the dimension could then be a future step.

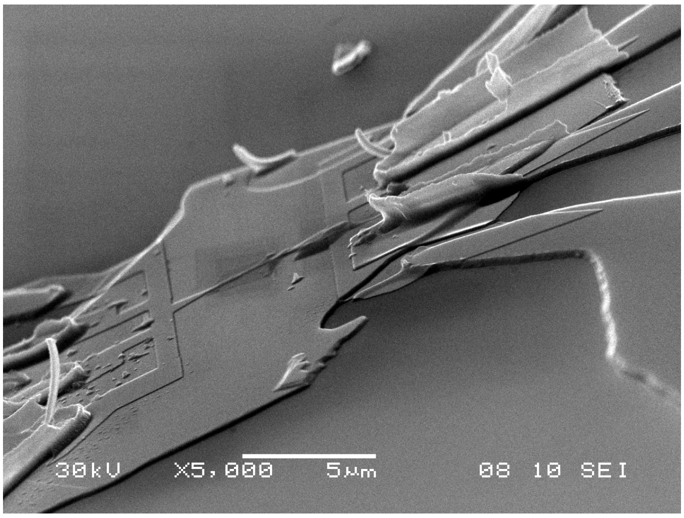

Figure 3.4: SEM image of a single Josephson junction on a BSTS flake (made by positive lithography, 30 nm Nb junction, 200 nm Nb leads). The ears are pronounced on the part of the leads that overlap the BSTS, suggesting BSTS plays a role in the formation of the ears. This image shows clearly that it is necessary to remove the ears before starting the e-beam procedure.

FIB lithography

With the e-beam it was initially challenging to make short junctions of high quality. Therefore some experiments were done with the Focused Ion Beam (FIB). The FIB has a maximum resolution of 7 nm at a maximum accelerating voltage of 30 kV [48], and would be ideal for making small junctions in niobium leads on top of BSTS.

The tests with the FIB showed that it was not possible to make the junctions deep enough, without melting the BSTS, see Figure 3.5(a). BSTS is, like most bismuth chalcogenides, a thermoelectric material [12], which means that it creates a temperature difference under an electric potential and vice versa. Their (perpendicular) thermal conductivity is poor. So the likely explanation is that under the high beam current of the FIB, the BSTS starts to heat, but cannot conduct this heat very well and starts to melt.

Also during wire bonding, or during measurements in the bath cryostat, the BSTS melted, see Figure 3.5(b,c). Wire-bonding is the process of connecting the leads of the sample with thin aluminum wires to the pads on the sample holder of the measurement set-up. The melting of BSTS is attributed to static discharge. In the bath cryostat this might result when changing the measurement cables, without the possibility to ground the sample first. During static discharge a large current passes trough a small area of the BSTS via the Josephson junctions, melting the BSTS locally. In next samples this problem was solved by grounding the samples and the wire bonder. In the Triton measurement set-up the sample can also be grounded when changing the cables.

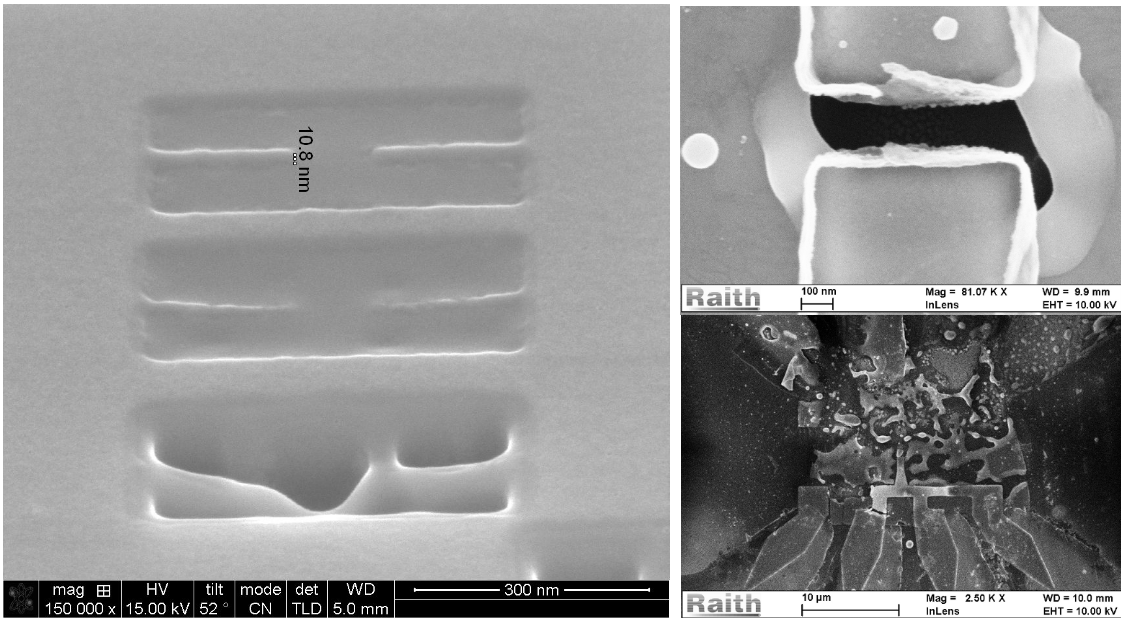

(a) (b) top and (c) bottom

Figure 3.5: (a) SEM image of a few test lines made with the FIB on a niobium lead on top of a BSTS flake. The lines are 10, 15 and 20 nm deep, which is not enough to go through the niobium. The last line is deformed, most likely due to melting of the BSTS. (b) A small part of BSTS is melted in a Josephson junction, probably due to a static discharge during wire bonding or measurement in the bath cryostat. (c) Severe melting of BSTS after a current of 20 mA was passed through the (top) niobium bar connecting the (top) leads.

3.2.2 Gold contacts on CuBiSe

The $Cu_{0.25}Bi_2Se_3$ crystal was received at the end of December 2012 and was then already, at least, four months old. In Amsterdam they measured superconductivity in the crystal below 3.8 K, by measuring via silver painted leads on the top of the crystal.

Compared to BSTS the cleaving of CuBiSe is quite difficult: especially the first layers of a new crystal results in small, rough and thick flakes. After several cleavings on the crystal, the quality of the flakes becomes better. Also the available crystal of CuBiSe was much smaller then the BSTS crystal. The difficulty in cleaving the CuBiSe could be an indication about the way the Cu^{+} ions are embedded in the crystal, either by random substitution of Bi or intercalation between the Se layers [17, 18], or it could just be an indication of a degradation of the surface. This will be further discussed in Chapter 6.

Because CuBiSe should be superconducting of its own, which was tried to be verified, gold leads were deposited instead of niobium. Niobium is a superconductor and could influence the measurements due to the proximity effect. A drawback is that gold lift-off is even more challenging than niobium lift-off on flakes. Lift-off with 1.7 and 3.5 µm positive photoresist in acetone and subsequently flushing with acetone and ethanol gives bad results, image reversal photoresist with the same lift-off procedure gives good results in combination with softly sliding the sample over a acetone drenched (lens) tissue and less gold deposition: approximately 119 nm instead of 159-199 nm. Especially in the case of gold deposition the removal of gold remainders with the tissue method is quite time consuming and can damage or remove the flake, but it is in some cases a necessary step.

Deposition of gold is done by a RF sputtering process, consisting of depositing a thin layer of titanium before sputtering the gold, the sputtering conditions are shown in Appendix B.2. Gold is deposited on titanium in order to have a good adherence between the gold leads and the substrate.

3.2.3 Niobium-gold junctions on BSTS

A few samples were made with junctions with niobium on one side of the junction and gold on the other side. The procedure is almost identical to the ones sketched above. First 200 nm niobium leads with a thin top layer of palladium were deposited on a suitable BSTS flake by image reversal photolithography and sputtering. The ears were removed from the leads before the next deposition step. Second, the gold part of the junction was deposited following e-beam lithography. The least fragile part of the junction was chosen to be gold, and was done first, because lift-off of gold is more challenging then lift-off of niobium. The third and last step consisted of matching and writing the second part of the junction with the e-beam and depositing 80 nm niobium.

The quality of the junctions on the samples were checked with the SEM. On some samples the two parts of the junctions were too much misaligned, one sample had only a slightly mismatch and was used for measurements. A SEM image of this sample is shown in Figure 3.6.

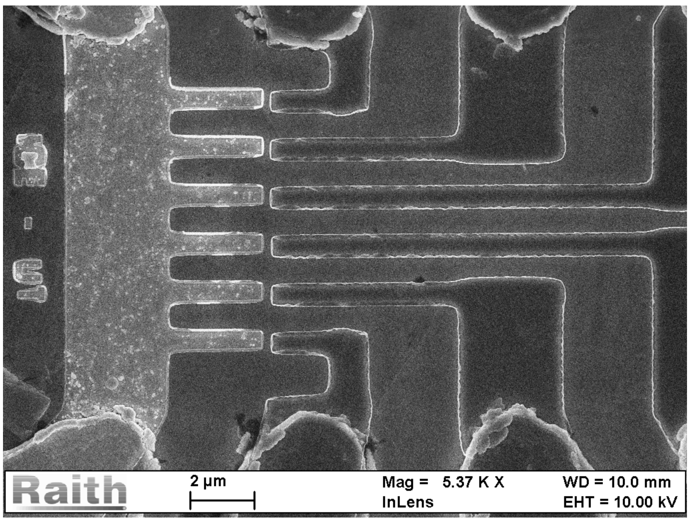

Figure 3.6: SEM image of six Au-Nb junctions on a BSTS flake, the bright part of the junctions is about 120 nm gold, the other 80 nm niobium The junctions are slightly shifted. Relatively small ears are shown on every part of the junction.

3.3 Status and future

At the moment this report was written still some challenges in the manufacturing have to be overcome in the future. In image reversal lithography bubbles are formed sometimes, after the first exposure. The bubbles are most likely due to the degassing of nitrogen from the photoresist during exposure. Several solutions are proposed in [50], but since the recipe was not changed and gave good results in the past, it is assumed that the new wafers cause the problems.

Two samples with Josephson junctions were measured, this will be discussed in the next chapter. SEM images were made after the measurements, and it turned out that the superconducting junctions were niobium shorts. Although some junctions, that looked alright in the SEM, had been prepared with the same settings, it turned out that these settings were not good enough for the smallest two junctions (50 nm and 100 nm) of these samples. This can be partly attributed to the large ears formed on the boundaries of the Josephson junction and to an apparent overexposure of the e-beam, probably due to too much scattering in BSTS.

Chapter 4

Measuring Josephson effects of Nb shorts on BSTS

In this chapter the results of the measurements on the superconducting Nb-BSTS-Nb junctions of two samples, numbered 52 and 49 (in order of measurement), are discussed. Each sample consists of six junctions with varying junction lengths, see Figure 3.3. The superconductivity turns out to originate from weak links, mainly from niobium ears formed after lift-off. The manufacturing of these samples is discussed in the previous chapter. Only the two smallest junctions were superconducting, the other longer and resistive junctions will be discussed in the next chapter.

4.1 Characterization and measurements

Both samples were measured in a Triton dilution fridge. The set-up is schematically shown in Figure 4.1. Four-point transport measurements were carried out on every junction of the two samples.

Previous samples had been measured in a liquid helium bath cryostat, but these samples did not show superconductivity for temperatures as low as 1.5 K. They gave resistances over the junction in the order of 10^2 Ω. In order to see supercurrents in BSTS, transport measurements were preformed in the Triton at temperatures down to 20 mK. At these lower temperatures the (proximity) normal coherence length [22] increases and, as a consequence, the maximum Josephson current increases also, making it easier to obtain and measure a Josephson current. Later, it was realized that the absence of a supercurrent in previous samples was probably caused by melted BSTS, as discussed in Section 3.2.1.

The measured samples had both six junctions with a designed length of: 50, 100, 150, 200, 250 and 300 nm. The width of these junctions was designed to be 300 nm. All transport measurements were carried out using a four-point measurement, and magnetic fields were applied perpendicular to the sample surface. Because of the time evolution of BSTS' transport properties and just as a sanity check, most of the junctions were measured two times, with a reasonable period of time in between (a few days to a few weeks). The overall behaviour of the junctions did not change.

Almost all measurements in the Triton involved a current sweep from zero to negative currents, then trough zero to positive currents and back to zero again. In this way the reproducibility of the measurement can be checked. The voltage over the junction and the differential resistance were measured, the applied magnetic field was also registered.

When the system was brought to reasonable high fields, vortices might have entered the hybrid devices reducing the critical current of the superconducting parts of the sample. Since niobium is a type-II superconductor, magnetic flux starts to penetrate into the superconduc-

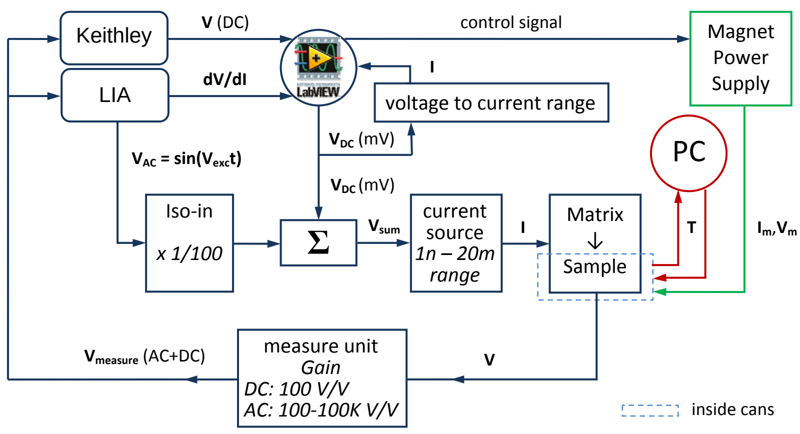

Figure 4.1: Schematic overview of the Triton dilution fridge measurement set-up. The Keithley does a voltage measurement, while the Lock-In Amplifier (LIA) measures the differential resistance. The measurements are controlled by a PC via the LabVIEW software.

tor above its first critical field B_{C1}, although the (internal) superconductivity will not be destroyed until a much higher second critical field B_{C2} is reached. Therefore the system was heated above the critical temperature $T_c \approx 9.2$ K of niobium, at these instances. Only at some early measurements on sample 52 and 49 this was omitted, since B_{C1} was not determined then.

In the present case the niobium of the device reaches its resistive state at about $B_{C2} \approx 3$ T (measured at the 100 nm junction of sample 52). The observed Fraunhofer patterns, which will be discussed later on, becomes very rough above 0.14 T, this is most likely due to the movement of vortices and is therefore an indication that B_{C1} is reached.[1]

4.2 Superconducting shorts as Josephson junctions

Superconductivity was measured in both samples on junctions with a designed length of 50 nm and 100 nm. The characteristics of both samples are globally the same in behaviour. Between comparable measurements on the same sample there does not seem to be much difference, but between different samples there is. For example, the 100 nm junction has a critical supercurrent (at zero magnetic field) of about 150 µA, while on sample 49 does not even reach 100 µA, see Figure 4.3. It should be noted that the supercurrent of the 50 nm junction at zero magnetic field (sample 52 and 49) could not be measured, it was outside the range of the measurement set-up.

4.2.1 I, V-curves

In the obtained I, V-curves, both the first traces on either side of the origin differ from their traces back, resulting in a hysteresis, see Figure 4.2. This was also observed in the S-TI-S junction of [51], but they did not have an explanation for this effect. We think this difference is likely caused by electron heating (hot electrons). Electron heating in the resistive state, without heating the sample, results in a smaller critical current on the way back to

[1] As a sanity check for the value of $B_{C1} \approx 0.14$ T it follows from $B_{C1} = \frac{\phi_0}{4\pi\lambda^2} \ln\left(\frac{\lambda}{\xi}\right)$ and $B_{C2} = \frac{\phi_0}{2\pi}\frac{1}{\xi^2} \approx 3$ T that $\xi \approx 10.5$ nm and λ lies between 11.8 nm and 39.5 nm at $T \approx 30$ mK. Although both parameters are temperature dependent their ratio $\kappa = \lambda/\xi$ is not, and close to unity according to the literature [22], therefore λ is most likely to be 11.8 nm. Since these values of λ and ξ are in the same order of the the values found in the literature [22], the value of B_{C1} is thus not unrealistic.

the origin (retrapping current), as was observed by Courtois and colleagues [52] in normal (in-plane) S-N-S junctions. These junctions have a small capacitance, therefore it is unlikely that the hysteresis is due to a capacitance in the sense of the RCSJ-model (Resistively and Capacitively Shunted Junction) [53, 22]. Our superconducting junctions also have a small capacitance since they turned out to be shorted, this will be discussed later on. From now on only the first traces on either side of the origin are used and shown in graphs, because the effect of heating is then minimal.

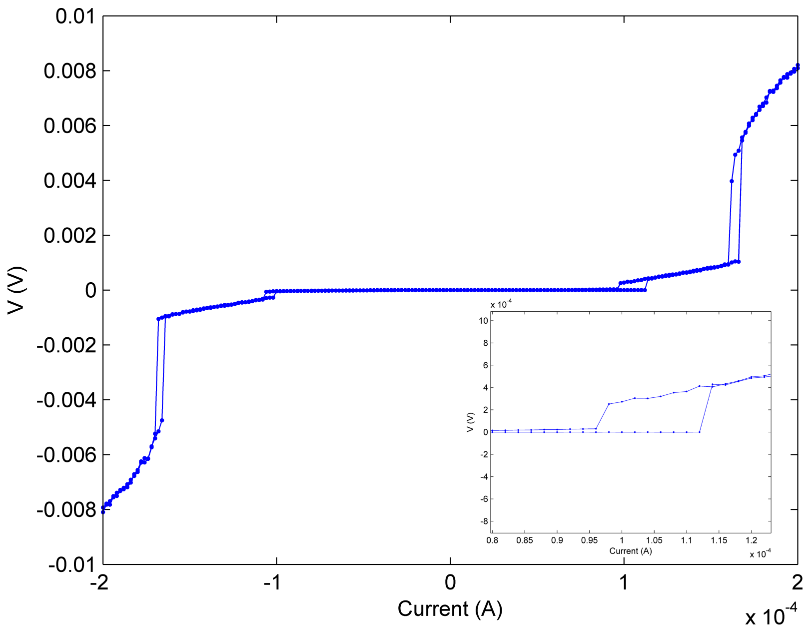

Figure 4.2: A typical I, V-curve for a superconducting junction, in this case from the 50 nm junction on sample 49 at 13 mT. The inset shows a zoom of the hysteretic behaviour at the critical current on the right side of the origin. The retrapping critical current is smaller due to heating (hot electrons).

The maximum supercurrents are asymmetric in the I, V-curves with respect to the origin. This is expected to be due to the self-field induced by the current that is passed trough the device, therefore the effective magnetic field differs from the applied field. The self-field has a different direction for positive and negative currents. Therefore th corresponding I, V-curves will have a different critical current for negative and positive applied currents, since the effective field is different in both ranges. This asymmetry is also observed in the graphs of Figure 4.3.

4.2.2 Fraunhofer pattern and SEM

In non-zero magnetic fields it was possible to suppress the critical currents, resulting in a modulation of the critical current of these junctions. This modulation has signatures of a Fraunhofer pattern, but it is at least superimposed on another oscillation or distorted. In three measurements a modulation could be determined (on 50 and 100 nm junction on sample 49, and on a 100 nm junction of sample 52), see Figure 4.3. A modulation period of about 0.04 T can be observed in these graphs. This modulation is a proof of the Josephson nature of the supercurrent across the junctions.

Although the area of the 100 nm junctions should in principle differ from the 50 nm

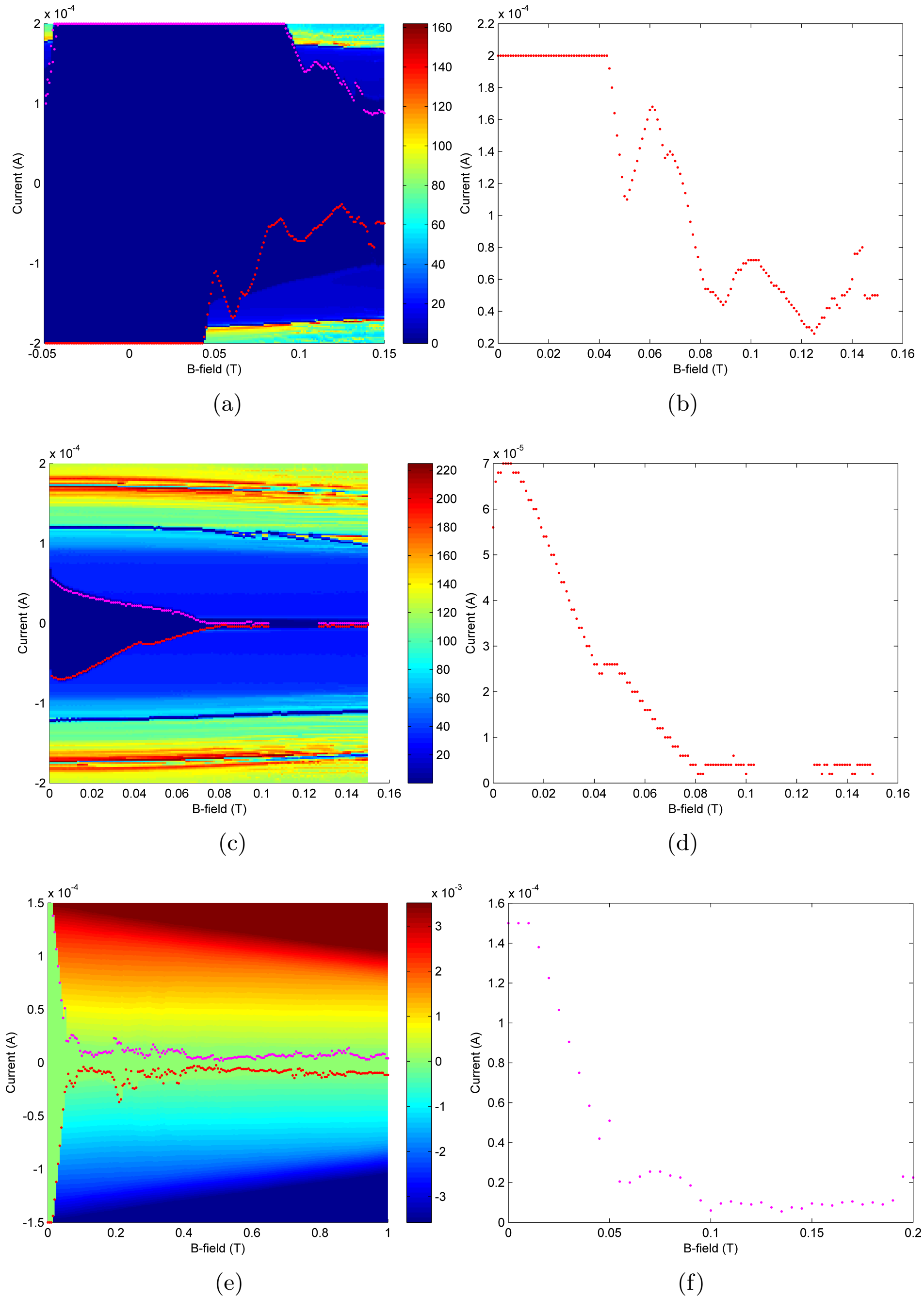

Figure 4.3: Dependence of the supercurrent on magnetic field, the colour scale indicates resistance for all but the last 2D-graph, where it indicates voltage. In the 2D-graphs the onset of the supercurrent is indicated with red and magenta markers (at the negative and positive part of the current sweep, respectively). Next to the 2D-graphs, for every measurement sweep only the first transition of superconducting to the normal state is plotted (absolute value). This first transition is the least effected by electron heating (hot electrons), since before the start of every new current sweep, some time is waited for the system to reach its equilibrium. Graphs (a-d) show measurements on sample 49 of respectively the 50 nm and the 100 nm junction; (e,f) are measurements of the 100 nm junction on sample 52. For sample 49 the current was first swept to negative currents and then to positive currents, for the 100 nm junction of sample 52 this was the other way around. The graphs show the modulations of the supercurrents, the modulation is always more or less 0.04 T. The oscillations deviate from the ideal Fraunhofer pattern. The indicated junction lengths are the designed lengths.

junctions, they also show a modulation of about 0.04 T. This would suggest from[2]:

$$L + 2\lambda = \frac{\alpha\phi_0}{W\Delta B}, \tag{4.1}$$

where ΔB is the modulation period, that both junctions have about the same length L, which should not be the case unless $2\lambda \gg L$. Also, no good fits can be made to these graphs with the theory described in Section 2.1.1. This can partly be explained by the fact that the Fraunhofer pattern will be distorted because the critical current is reduced due to (magnetic) flux trapping in the niobium above its first critical field. This is caused by the moving of the vortices of these fluxes, which result in dissipation [22]. This can result in a distortion of the shape of the pattern, a damping of the oscillations or a shift of a pattern [54].

SEM images made after the measurements revealed that the junction dimension were different then intended with the design. The junction width turned out to be 434.93 ± 6.29 nm for the junctions on sample 52 and 401.96 ± 28 nm for the junctions on sample 49. A few examples of the SEM images are shown in Figure 4.4. Also the junction lengths differed from the designed lengths, as indicated in Table 4.1. These dimensions were verified by SEM after doing the measurements, instead of before, in order not to damage or influence the surface states. During SEM it was also found that some junctions were (possibly) shorted due to large ears, due to an underexposure or due to bad lift-off, the junctions are indicated red or orange in Table 4.1.

From this we must conclude that all superconducting junctions are probably junctions with weak links of niobium ears, or a constriction of niobium, which explains why we do see a Josephson supercurrent. Since both give rise to Josephson effects. Furthermore, from the SEM images it is not expected to have a good Fraunhofer like pattern because of the non-ideal (irregular) shape of the weak links (ears) or the microbridge junctions [15, 57]. A constriction forming a microbridge – which could be the case in Figure 4.4 (b) – shows Josephson effects, which can be explained by the motion of Abrikosov vortices at the narrowest point of the bridge [55]. Under influence of the Lorentz force the vortices can be pulled in and out of the superconductor, the movement of the vortices induces an electric field and thus dissipation [56].

This could also explains the resemblance in the Fraunhofer oscillations of different sized junctions, since now $2\lambda \gg L$, so all shorted junctions have the same area. With this knowledge it is most likely that the hysteresis in the I, V-curves is caused by heating instead of a shunted capacitance, as discussed in the previous section, because in a shorted (or weak link) junction no insulator is in between that can contribute to a capacitance.

All other junctions were not shorted but they were not superconducting. These resistive junctions will be discussed in the next chapter.

Designed (nm)	Sample 52 (nm)	Sample 49 (nm)
50	74.49	-
100	151.3	48.29
150	<183.3	52.59
200	140.7	149.0
250	168.4	204.9
300	250.9	232.3

Table 4.1: Junction lengths designed and realized per sample and junction (approximately), red means shorted junction, orange means possibly shorted junction. Due to the large ears and strange shapes of the junctions it is difficult to determine the exact length.

[2]This equation is derived from the Fraunhofer sinc-function in Appendix C. Here α and ϕ_0 are constants defined in the referred Appendix, and W is the junction width, which is about the same for every junction.

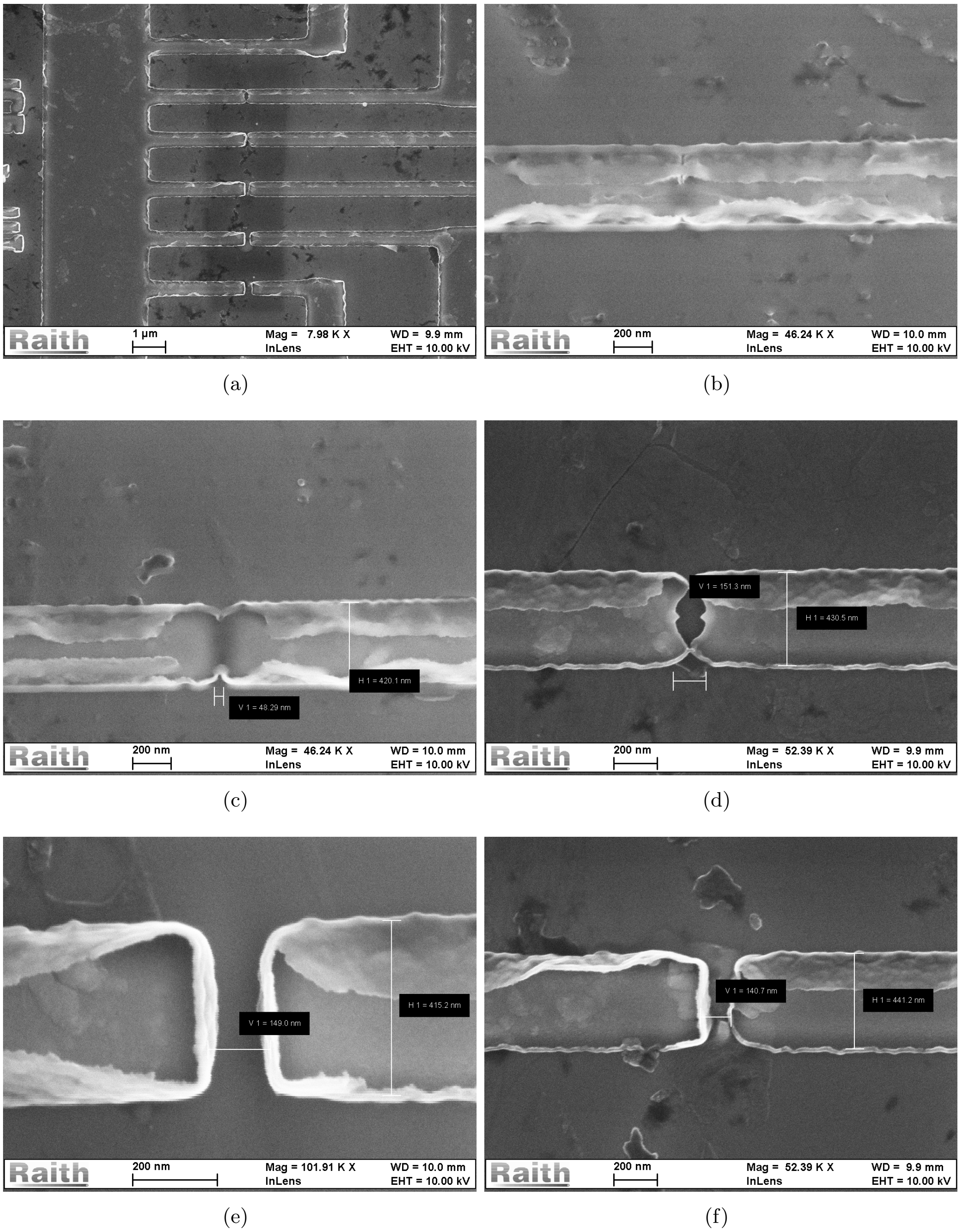

Figure 4.4: A few SEM images of the junctions measured in the Triton, in all cases are the junctions smaller than expected. Figure (a) shows an overview of the junctions on sample 52, (b) shows the 50 nm junction of sample 49, (c,d) show the 100 nm junction of sample 49 and 52 respectively and (e,f) show the 200 nm junction on sample 49 and 52 respectively. The superconducting junctions (50 nm and 100 nm of both samples) are shorted with probably a weak link of niobium (ears) in between, causing the observed Josephson nature of the supercurrent. The indicated junction lengths are the designed lengths.

4.2.3 Flux-flow

Above the critical current, a normal resistance appears. Sometimes it is impossible to speak about 'the' normal resistance of the junction, see for example Figure 4.3 (a) and (c), which shows non-uniform normal resistances. This manifests in peaks in the resistance and kinks in the I, V-graphs, a striking example is shown in Figure 4.5.

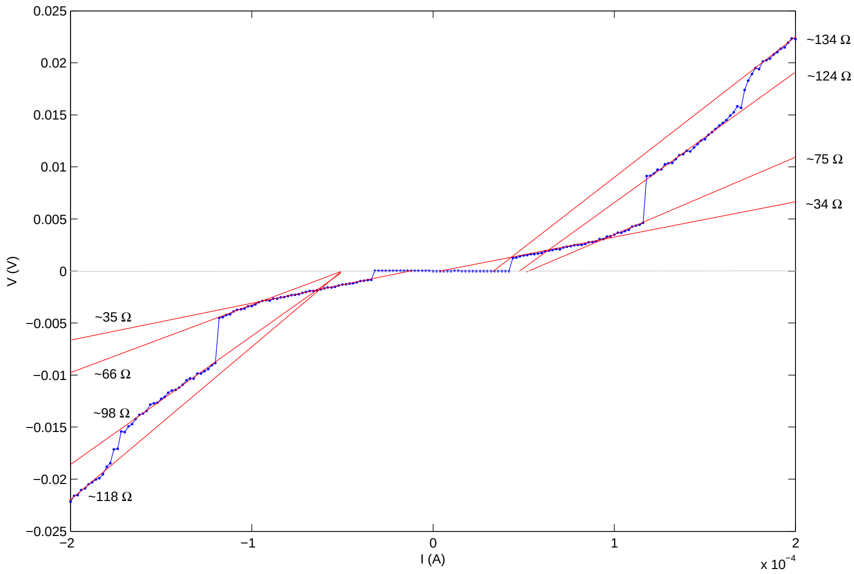

(a)

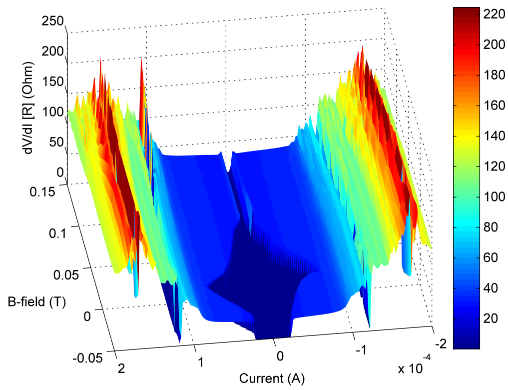

(b)

Figure 4.5: Measurements on junction 100 of sample 49 (second measurement) shows many kinks in the (a) I, V-graph at -26 mT and (b) peaks in the resistance. The hysteresis in the graphs was removed by only plotting the first trace (as discussed earlier). In (a) the red lines are tangent lines to to the different slopes of the graph, the numbers next to these lines indicate their slopes.

In the previous section the possibility of a constriction (microbridge) was discussed. It is known from the literature that a microbridge can show Josephson effects when the width of the bridge W_b is comparable to, or smaller than the effective London penetration depth ($\lambda_\perp$) [56]:

$$\lambda_\perp = \lambda_L \text{cotanh}(d/2\lambda_L), \tag{4.2}$$

where λ_L is the London penetration depth (from literature $\lambda_L = 40$ nm for Nb [22]) and d is the film thickness of the bridge.

In a microbridge vortices can cross the bridge under influence of a magnetic field, this vortex flow results in resistance. With the opening of an additional vortex flow channel the resistance increases [58, 56]. The resistance when n channels are present equals n times the resistance of one channel. This results in an increasing slope with integer values. This behaviour is approximately observed in the present case, as shown in Figure 4.5(a). The red lines are tangent lines to the data and their corresponding slope is give by the resistance next to the line. All slopes (up to the last one) are approximately multiples of the first slope. This is an indication that we are indeed dealing with microbridge for the present junction.

The assumed microbridge, shown in Figure 4.4(c), has a width of $W_b \approx 288.57$ nm, which is also the lower limit of $\lambda_\perp$. Using Eq. 4.2 with the aforementioned values one finds a maximal thickness of the bridge of $d \approx 11.2$ nm. Noting that the area of assumed microbridge appears much darker in the SEM image, it is realistic that the thickness is much smaller that the 80 nm deposited Nb leads, and $d \approx 11.2$ nm is reasonably possible.

An alternative or complementary explanation for those multiple peaks and kinks is the assumption that certain parts of the junction get superconducting in a different stages in the measurement. The two superconducting jumps in Figure 4.5 might be an indication for this. It could be due to different parts of the junctions becoming resistive at different currents, for example first the weak link and then the niobium leads, or it could also be a combined effect of a proximity induced superconductor junction in the BSTS and the niobium weak link.

4.3 Resistive junctions

All other four junctions, labelled by there designed junction length, 150 nm, 200 nm, 250 nm and 300 nm, were not superconducting. Nevertheless, they give rise to interesting effects. All these resistive junctions showed a large zero-bias resistance peak and in some cases other side peaks were also observed. The results of these resistive junctions will be discussed in the next chapter.

4.4 Discussion and outlook

The measurements and the SEM images show that it is very hard to make good quality junctions, which was also noted in the previous chapter. For a good S-TI-S junction, operating at 2 K, the junction length should be less than $\xi_n \approx 30.5$ nm, which follows from the 'dirty limit' normal coherence length Eq. 2.4. The values for the calculation, $v_F \approx 4.6 \cdot 10^5$ m/s and $l_e \approx 10$ nm, were known from Hall measurements[3] at about 2 K. The 'dirty limit' applies since the calculated coherence length at 30 mK, $\xi \approx 10.5$ nm, is about the same as the mean free path at 2 K. Since at 2 K the coherence length will be larger (since it increases with increasing temperature), $\xi > l_e$ and since we have diffusive transport the 'dirty limit' will apply then.

Using the same parameters at the Triton operating temperature of $T = 30$ mK, givens $\xi_n \approx 250$ nm, which would indicate that we should have measured superconductivity in at least one of the longer junctions, which turns out not to be the case. The parameters mentioned above are measured on a different flake, but it is not expected that they deviate very much (within an order of magnitude). Therefore, from the knowledge that the junctions with $L \geq 140$ nm are resistive, it can be assumed that is $\xi_n < 140$ nm.

Therefore it is necessary to make either good quality smaller junctions, which is challenging, or improve the mean free path of BSTS, giving rise to a larger normal coherence length which makes it able to work with larger junctions. The mean free path can be enhanced by tuning the composition of BSTS. In order to get a large insulating bulk, the disorder in BSTS

[3] M. Snelder is kindly acknowledged for these measurements.

by charged defects was increased by tuning its composition to maximum bulk resistivity. It would be interesting to find a good compromise between optimal bulk resistivity and optimal mean free path.

In the present case SEM images were made after all the measurements series in order to protect our samples. Since Josephson effects were measured it was not expected that the junctions were not good. Therefore in the future, considering the time it takes to make, measure and analyze the samples[4], it might be worthwhile to investigate if the SEM really has a large impact on the quality of the BSTS. If PMMA resist is on top of the sample during SEM the BSTS might be protected enough.

As a closing remark, the difficulties in sample preparation are noted. The quality of the samples and the time spent on making them will be highly improved if it becomes possible to grow high quality layers of BSTS. A few groups worldwide are able to grow BSTS, already. In this way junctions can be deposited first on a suitable insulator, ears can be easily removed without the risk of removing the flake and the dimensions can be checked with the SEM before measurements. Finally a topological insulator can be grown on top.

4.5 Conclusions

Four-point transport measurements on Nb shorts on BSTS were carried out at low temperatures, in the order of 30 mK and magnetic fields up to 3 T. Supercurrents through 50 nm and 100 nm weak-link shorts were observed in both samples 49 and 52. After the measurements, SEM images showed that these superconducting junctions are shorts of niobium (ears), forming weak links or microbridges. The observed Fraunhofer modulation can be assigned to these hybrid structures. Due to the niobium weak links the shunted capacitance of the junction is too low to explain the observed hysteresis in the I, V-curves (and differential resistance). We explain that this hysteresis is likely caused by electron heating (hot electrons).

[4]At least a week to make samples, about half a day for loading the Triton, about two days for cooling down, about a week to measure a whole sample, two and a half day to warm-up and unload again and a few days to analyze the data. Thus, all in all about a month. Also note that it is not easy to get time on the Triton.

Chapter 5

Measuring resistive BSTS junctions and hybrid devices

This chapter continuous the discussion of the measurements in the Triton, as discussed in Section 4.1, for the non-shorted, resistive junctions on sample 49 and 52. During the characterization of these samples it was found that most of the junctions on sample 49 and 52 (junction 150, 200, 250 and 300) were not superconducting within the resolution of our measurements (ranging from 20 nA to 0.5 µA). A clear resistance peak around zero voltage (and zero applied current) was observed. This peak grows with magnetic field, and is fairly symmetric around the origin. At the same time no significant changes in slope of the straight I, V-curves were observed. These peaks will be referred to as Zero Bias Resistance Peaks (ZBRP). The ZBRP are not due to a zero-point singularity since they have a reasonable width and the gradual up- and down turns consists of several data points. In sample 52 also side peaks were observed at different biases. Typical measurements are shown in Figure 5.1.

5.1 Magnetoresistance

A positive magnetoresistance is observed for all resistive junctions. This can be most clearly observed in the ZBRP, where the resistance is the highest, a typical curve is shown in Figure 5.2.

Weak antilocalization (WAL) is a well known effect in BSTS as discussed in Chapter 1 and 2, and the observed magnetoresistance curves look very similar to magnetoresistance curves due to WAL. In thin flakes surface-dominated transport through the 2D metallic surface states is expected, where WAL is caused by the π-Berry phase picked up by the electrons upon reflecting on an impurity [13, 15]. Also the bulk spin-orbit coupling could give rise to WAL. Xia and co-workers [13] found that in bulk single crystal samples this 3D bulk contribution leads to a clear deviation of the (2D) HLN-fit to the measured curve.

To check whether or not WAL is observed in the present case, we numerically fitted the HLN equation (Eq. 2.7) to the relative conductivity peaks at zero voltage. Fitting parameters are the constant α and the phase coherence length L_ϕ as discussed in Section 2.4.1. The graphs are shown in Figure 5.3. The HLN equation applies for WAL in a 2D system, as is expected to be the case here for surface-dominated transport.

It turns out that none of the fits has the ideal value of $\alpha = -0.5$ per surface, as listed in the tables of Figure 5.3, although the values were always negative, which also means that weak localization (with $\alpha = 1$) can be excluded [15]. Because the fits with the HLN equation are very good, that is, the shapes correspond; it can be assumed we are dealing with WAL. It is likely that it is mostly due to the surface states since the bulk of BSTS is insulating at

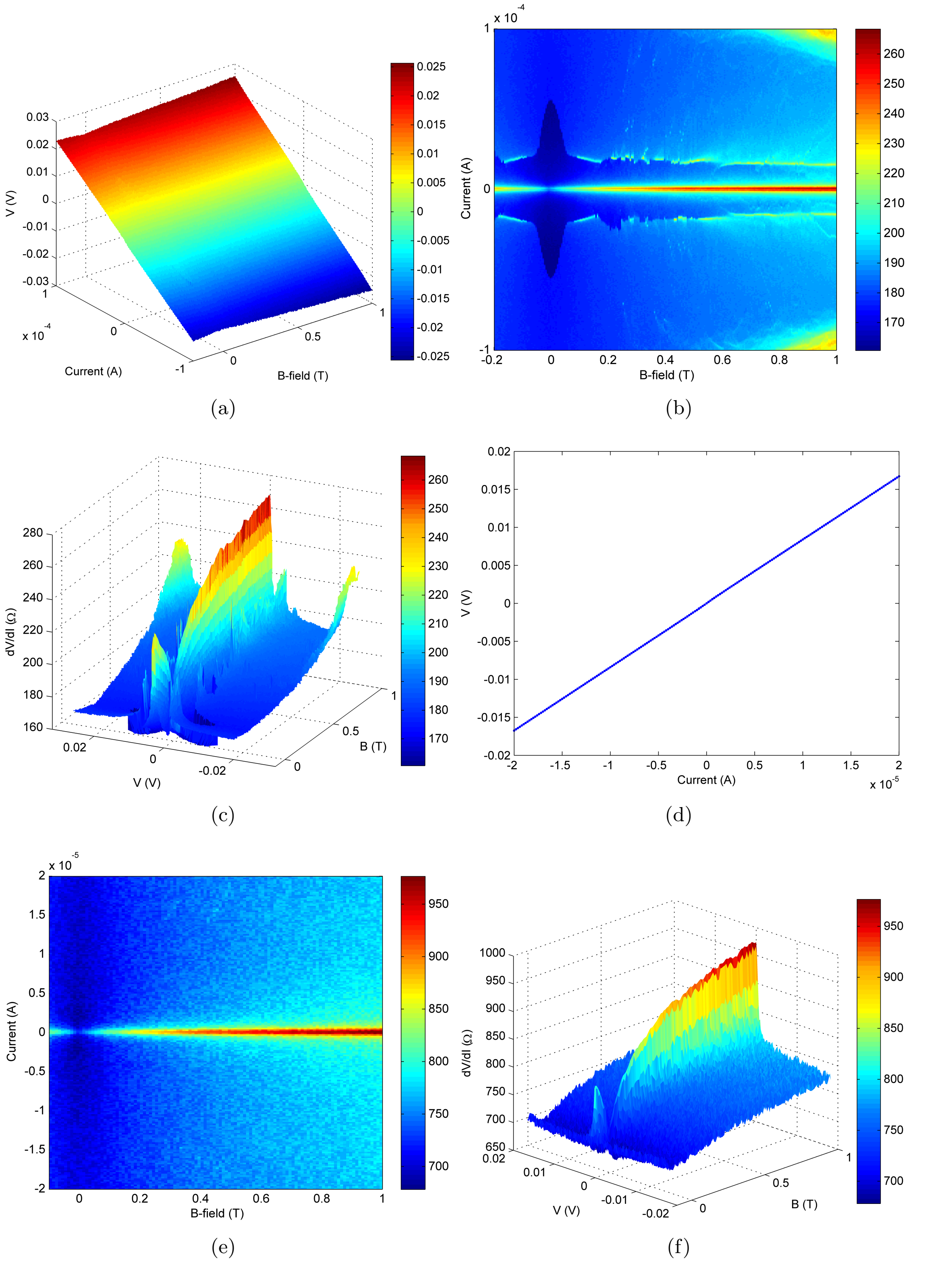

Figure 5.1: Two series of typical measurements on junction 150 of sample 52 (a-c) and junction 250 of sample 49 (first time measurement) (d-f). Although no steps can be seen in the I,V-curves, a clear peak is observed in the I,R,B and V,R,B-graphs at zero current (zero bias). The peaks grow with magnetic field and have a minimum at zero field (positive magnetoresistance). In some cases side peaks are observed, as for junction 150 of sample 52 shown here. The I,V-curve shown in (d) is measured at $B = 150$ mT.

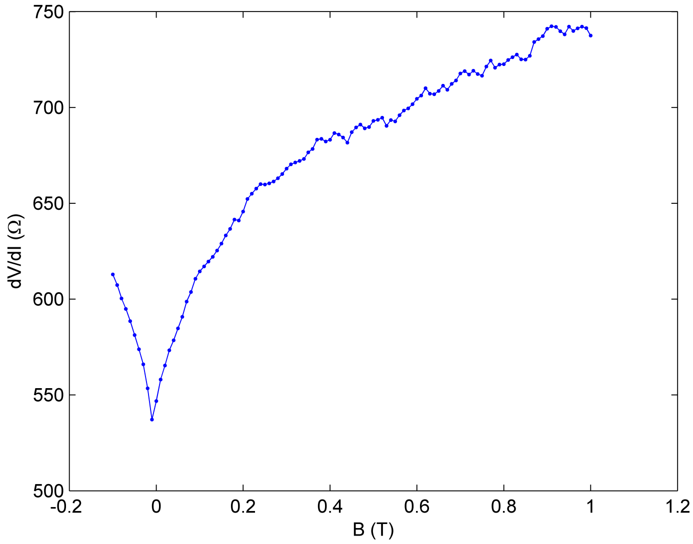

Figure 5.2: A typical magnetoresistance curve at zero voltage. This curve is measured on junction 300 of sample 49 (first time measurement).

low temperatures and the flakes are very thin (in the order of $\sim$ 100 nm). However, from the HLN fit this cannot be concluded, since the values for L_ϕ (assuming these values are correct[1]) are in all cases likely to be larger than the thickness of the flakes. This makes the system (surface states and bulk) effectively 2D, and thus no matter what the origin of the WAL, the 2D HLN will always apply. On the other hand, it should be noted that length of the junctions is also in all cases less than L_ϕ, which makes the system tend to 1D. This could be a part of the explanation why the α values deviate from the expected values, since the 2D HLN equation might not be fully applicable.

Since all junctions are on the same material you would in principle expect that all α and L_ϕ values (at least within a sample) have about the same value. This is not observed, although the shape of the magnetoresistance curves are identical, see Figure 5.4. In order to find possible explanations for these anomalous α-values of the HLN we analyze the junction system in more detail.

In the system, several series resistances contribute to the total resistance, as in:

$$R_{total} = R_{interface} + R_{BSTS} - \Delta R_{WAL}(B) \tag{5.1}$$

where $R_{interface}$ is the interface resistance between the Nb leads and the BSTS (the interface resistance of both Nb leads is accounted for in this resistance), and R_{BSTS} is the resistance due to the BSTS in between the junction. Both these resistances do not depend on magnetic field, and can be viewed as constants for a given junction. The correction on the resistance of BSTS due to weak antilocalization, $\Delta R_{WAL}(B)$, does depend on magnetic field. It is this part that contributes to the $\Delta\sigma$ of the HLN equation (since it fits to the change in conductivity due to a magnetic field).

In order to go from resistance to resistivity one has to multiply the measured total resistance with a geometrical factor $\frac{W}{L}$ for 2D conductivity, or $\frac{Wt}{L}$ for 3D conductivity, but

[1] Values of $\gtrsim$ 200 nm seems to be reasonable, it is at least comparable to the value Xia and co-workers [13] measured in the nearly identical $Bi_{1.5}Sb_{0.5}Te_{1.8}Se_{1.2}$: $L_\phi \sim 180$ nm at 2 K. Note that L_ϕ tends to infinity as $T \to 0$.

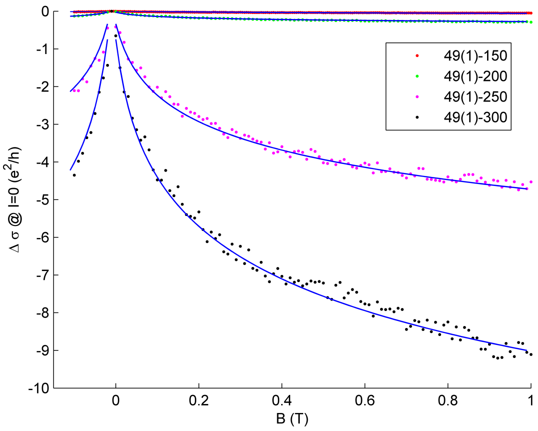

Junction	Length (nm)	α	L_ϕ (nm)
49(1)-150	52.59	-0.1	84
49(1)-200	149.0	-0.2	274.2
49(1)-250	204.9	-3.8	222
49(1)-300	250.9	-7.3	203.2

(a)

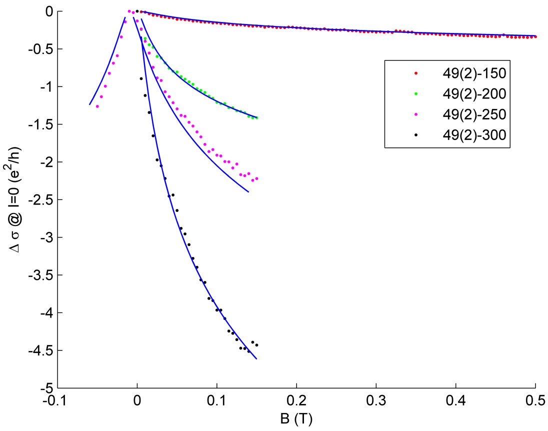

Junction	Length (nm)	α	L_ϕ (nm)
49(2)-150	52.59	-0.4	169.5
49(2)-200	149.0	-1.8	293.7
49(2)-250	204.9	-4.1	209
49(2)-300	250.9	-5.8	299.6

(b)

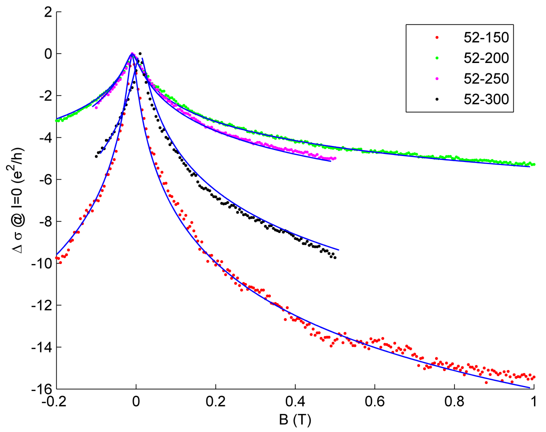

Junction	Length (nm)	α	L_ϕ (nm)
52-150	<183.3	-12.4	256.4
52-200	140.7	-4.5	223.3
52-250	168.4	-5.6	200.6
52-300	232.3	-9.8	213.7

(c)

Figure 5.3: The graphs showing the corrections to the conductivity at V=0 V for all junctions of (a) sample 49 first measurement, (b) sample 49 second measurement and (c) sample 52. The blue lines in the plots are the HLN fits to the measurements, the corresponding α and L_ϕ are listed in the tables. Sometimes it is hard to measure the exact junction length and width due to the ears and non-uniform shape of the junctions, the given lengths are therefore indications. The error bars are shown in Figure 5.5. If the length is chosen differently, α and L_ϕ will change accordingly.

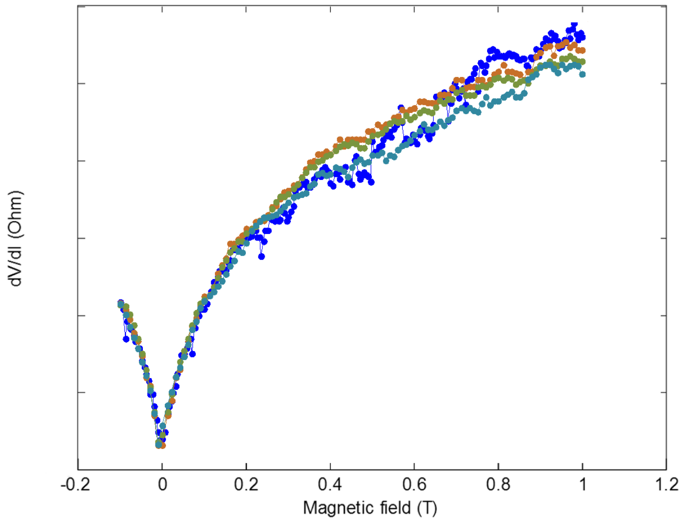

Figure 5.4: The magnetoresistance curves of the junctions of sample 49 (first measurement) are laid on top of each other, neglecting the difference in y-scale. One can clearly see that the curves have almost identical shapes.

this geometrical factor does not hold for the interface resistance.[2] Here, L is the junction length, W is the junction width and t is the thickness of the flake. Therefore, in order to get the right value for the conductivity relevant for the HLN equation, one should get rid of the interface resistance, which is an unknown value. Usually the interface resistance $R_{interface}$ is determined by scaling of the junction length. In those cases a larger junction length results in a larger R_{BSTS} contribution to the total resistance. Because at high magnetic field WAL is destroyed, one can plot the high field total resistance for different junction lengths and interpolate a linear fit. The offset will be the interface resistance $R_{interface}$, assuming that the shape and size of the Nb contacts stay the same.

In the present case the resistance of the BSTS junctions does not scale with the junction length (in the proper way), see Figure 5.5, therefore it is impossible to determine the interface resistance. Sample 52 scales non-linearly and sample 49 scales inversely with junction length. This makes it is impossible to disentangle the interface resistance from the conductivity. This is one of the reasons why the α and perhaps the L_ϕ values of the HLN fits do not match the predicted values and differ by a great amount for different junctions.

Several other possible explanations for the anomalous scaling and the deviations of the HLN fitting parameters can be thought of. First, we would like to refer to a report of Wang and colleagues [45]. They showed that in the case of Bi_2Se_3 in a magnetic field, the observed minimum in magnetoresistance at zero field, can only be explained by the additive contribution of WAL and electron-electron interaction (EEI). The EEI contribution in the relative conductivity, gives rise to an offset logarithmically with magnetic field and could thus affect the HLN fitting parameters, according to [44, 45]:

$$\Delta\sigma_{EEI+WAL}(B_\perp, T_0) \approx \\ -\frac{e^2}{h}\frac{1}{2\pi}\left\{\tilde{F}\ln\left(\frac{g\mu_B B_\perp}{1.3\mu_0 k_B T}\right) - 2\alpha\left[\Psi\left(\frac{1}{2}+\frac{\hbar}{4eL_\phi^2 B_\perp}\right) - \ln\left(\frac{\hbar}{4eL_\phi^2 B_\perp}\right)\right]\right\}, \tag{5.2}$$

[2]Let us assume here a reasonably homogeneous conductivity of the BSTS in the vicinity of the junction. Now, approximately all current passes through the junction area LW and the R_{BSTS} scales with $\frac{W}{L}$. Furthermore, one would expect the same interface resistance for every lead of all junctions, as long as the width and the shape of the leads stay the same.

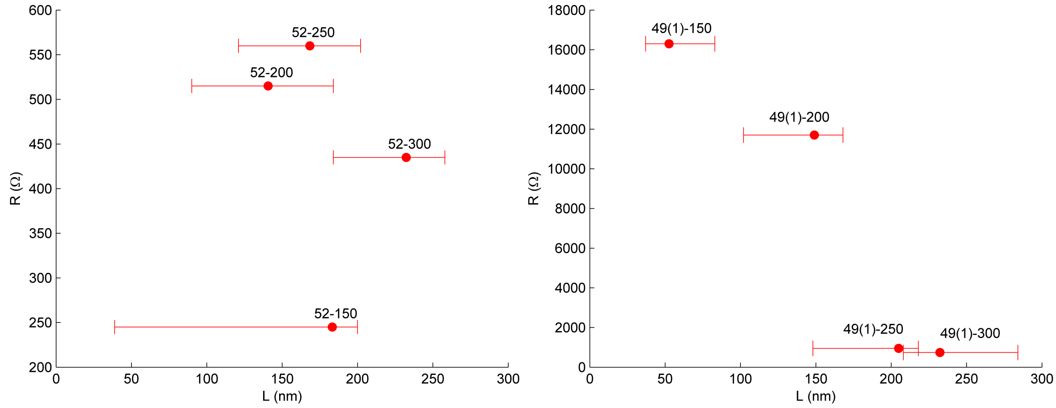

(a) (b)

Figure 5.5: Plots of the resistance against the junction length at 0.5 T for sample 52 (a) and at 1 T for sample 49, first measurement (b). Both samples do not scale linearly. The same behaviour was observed in the second measurement of sample 49. The data tips indicate the junction by its designed length.

see also Section 2.4 for details on the two terms in this equation.

The WAL-like behaviour can be observed in the magnetoresistance at all current biases. Therefore, a possible indication of a contribution of EEI is the increased peak in the magnetoconductance around zero voltage (EEI effects play a role in the vicinity of $V = 0$, as will explained in the next section), see Figure 5.6. The correction to the conductivity is the largest for zero voltage, it becomes less for larger absolute voltages. This can be possibly attributed to either (or both) EEI interactions that do not play a role anymore, or WAL that is reduced for higher voltages. The last follows from $\Delta\sigma_{WAL} \propto \alpha \ln(T) \sim \alpha \ln(V)$ (with a negative α for WAL) [45], which indicates that the WAL correction is reduced at higher voltages.

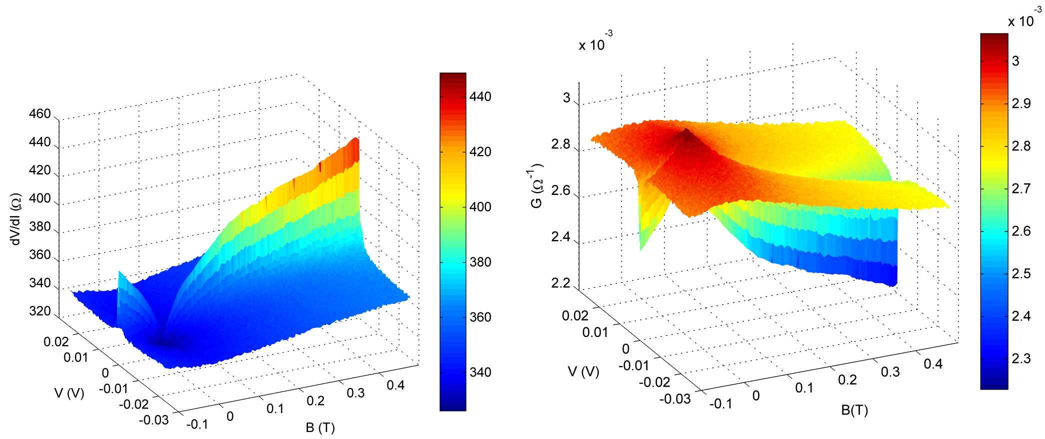

(a) (b)

Figure 5.6: The dip(peak) here attributed to WAL is observed over the whole spectrum of bias current in the $R, I, B(G, I, B)$-graphs of sample 52, junction 300 (a,b). Around zero bias voltage the dip(peak) extra large, which might be an indication of and EEI contribution.

Although we did some effort in trying to fit the combined contribution of WAL and EEI to the present data, this did not result in good fits, with more reasonable values of α and L_ϕ. Perhaps EEI could play a role in combination with one or more of the other possible explanations.

The most important and likely explanation is a (large) inhomogeneity (of the conductivity) of the flake, giving rise to difference up to one order of magnitude in the conductivity, which is reflected in the α and L_ϕ values and the absence or anomalous scaling. It could also lead to contributions of better conducting paths outside the junction, which do not scale with the junctions W and L, but do contribute to the WAL. A second thing one should realize is the fact that the Nb leads have large ears, and in some cases, an irregular shape. This makes it hard to determine the exact junction width and length, which has a large impact on the fitting parameters of the HLN equation, and could also affect the total resistance of a junction. In Section 5.3 we will further analyze the supposed inhomogeneity of BSTS.

5.2 Zero-bias peaks

In the literature Zero-Bias Conductance Peaks (ZBCPs) are observed in the tunnelling conductance of N-TI-S junctions [49]. They indicate the presence of Andreev reflection in a p-wave superconductor, giving rise to Andreev bound states, as discussed in Chapter 2. In the present case one could also expect such a peak since we deal with a resistive S-TI-S junctions, effectively acting as two p-wave SN contacts separated by a normal metal. We would like to stress that the present peaks are always in opposite direction, i.e. ZBRPs, see Figure 5.7(a) for a typical example. While the normal ZBCP might still be present, another process leading to the ZBRPs peaks obscures them.

Since no signs of ZBRPs are seen in the hybrid devices with superconducting shorts or weak links, as discussed in the previous chapter, it is likely that the ZBRP are caused by effects in the BSTS. In the SEM images of these ZBRP samples (see Figure 4.4(e,f) it can be clearly seen that the junctions are gapped, and thus electrons have to cross the BSTS. Since electron-electron interaction (EEI) are commonly observed in Bi-based topological insulators [15], it could be a likely explanation for observed ZBRPs. EEI give rise to an increase in resistance [15, 40], resulting in a peak in resistance (a dip in the density of states) around the Fermi energy E_F.

Although EEI is commonly observed, the present ZBRP has not been mentioned in the literature. In most cases EEI is used to explain a logarithmic decrease in conductance with temperature [15]. Since the temperature T can be related to energy, which can be related to voltage V, the EEI correction follows the same voltage dependence. The 2D correction due to EEI is a logarithmic dependence $\Delta\sigma_{EEI,2D}(T) \propto \ln(T)$ whereas the 3D dependence has a square root dependence $\Delta\sigma_{EEI,3D}(T) \propto \sqrt{T}$. A plot of a typical ZBRP graph, together with fittings of the 2D and 3D dependence shows clearly a 2D dependence, see Figure 5.7.

Both WAL and EEI follow the same voltage and temperature dependence [45], for 2D:

$$\Delta\sigma(T, H = 0) \propto \alpha \ln(T), \tag{5.3}$$

where T could equally well be substituted by V, as discussed earlier. We found from the HLN fits to the relative magnetoconductivity that α is negative, and thus it is due to WAL. The same α applies here if the ZBRP is due to WAL, but with a negative α this would lead to a dip instead of a peak in resistance. For EEI the α of the HLN does not apply and is now defined by $\alpha = (1 - \frac{3}{4}\tilde{F})$ [45], where $\tilde{F}$ is a screening factor between zero and unity [46], this gives always positive α values, and can thus explain the ZBRP.

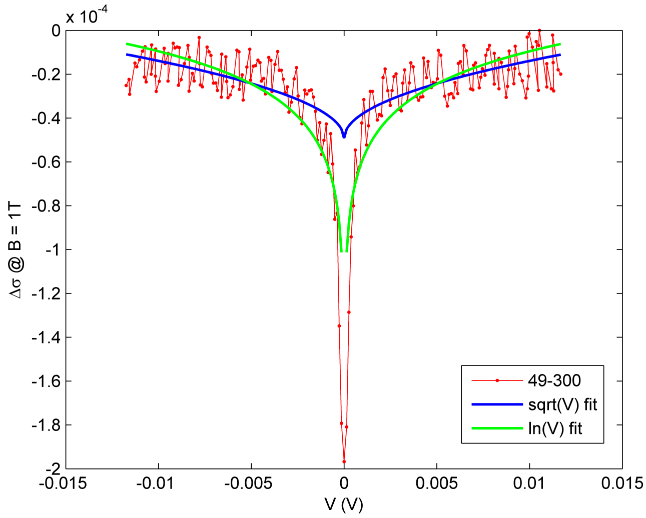

(a)

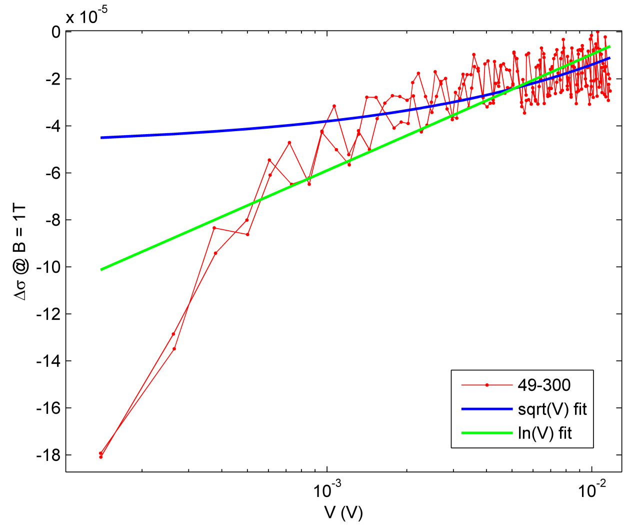

(b)

Figure 5.7: Fit of the 2D ($\ln T$) and 3D ($\sqrt{T}$) dependence of the EEI to the ZBRP of junction 49-300 at a magnetic field of 1 T, in a normal (a) and a semilogarithmic plot (b). The 2D dependence clearly fits the data bests. Note that the $\ln(0) = -\infty$, although this data point is not shown.

5.3 Side peaks

Another feature that becomes clear from the measurements is the existence of side peaks next to the ZBRP, see Figure 5.8. The height and position of those peaks differs within and between different junctions and samples, in the measurements of sample 49 they are not even present, or fell out of the measurement range (compare Figures 5.1 (b,c) with (e,f)). The positions of those peaks seem to shift to higher voltages (or currents) for larger junctions.

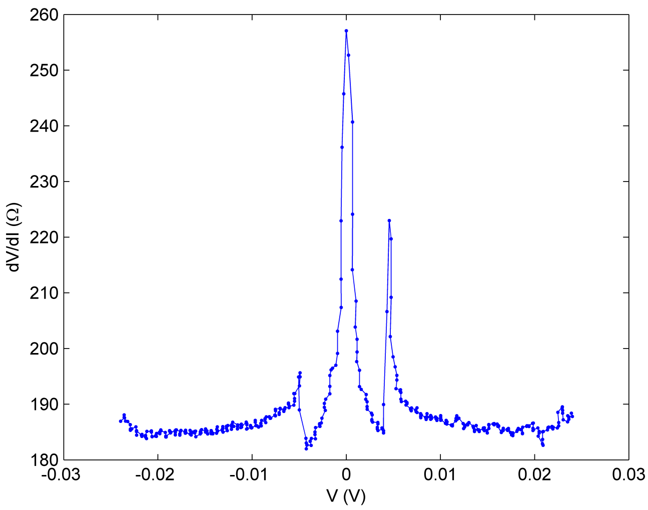

Figure 5.8: Side peaks in the differential resistance of junction 150 of sample 52 at 0.495 T.

Although speculative, the side peaks could be indicative of the superconducting gap edge of a p-wave superconductor. Then they can be explained if you assume the following situation: the superconducting Nb contacts induce p-wave superconductivity (pS) in a part of the BSTS via the proximity effect, thus effectively forming two p-wave SN contacts separated by a part normal BSTS (N): a S-pS-N-pS-S junction. When the device is biased with a voltage (current), a peak appears around zero voltage (current, E_F) due to EEI in BSTS. The side peaks appear due to the pS-N interface in the adapted BTK-formalism for (chiral) p-wave superconductivity of Eschrig, Iniotakis and Tanaka [25] (see Chapter 2). They showed conductivity dips in the tunnelling conductance of N-I-pS junctions (see Figure 2.3(c)) near the superconducting gap Δ. In the present case we are dealing with S-pS-N-pS-S junctions. Such a theory is, to our knowledge, not available, so future calculations and measurements have to show whether or not this is a valid assumption.

According to this p-wave BTK theory a resistance peak at the gap energy appears in the interface resistance. This peak depends on the strength of the barrier at the NS interface; a peak will be higher for stronger barriers. The shift of the side peaks to a higher voltage for longer junctions, can then be explained by the fact that the normal distance is larger, resulting in a larger voltage drop over the normal area. The S-pS-N-pS-S junction can be regarded as three resistances in series: two pSN-junctions and a normal resistance in between (as in Eq. 5.1 but without the WAL term). Therefore the voltage drops of the individual parts can be added. Due to the voltage drop over the normal BSTS, the side peaks resulting from the two pS-N contacts shift to higher voltages than their usual $2\Delta/e$ position (one Δ/e for each pSN-junction), the shift will be larger for longer junctions.

Since the positions of the side peaks depends on the length of the BSTS in the junction, we used this as an additional check for the scaling of BSTS. This analysis could only be performed on sample 52, since sample 49 showed no side peaks. Figure 5.9(a) shows the result. Here the corresponding voltages of the side peaks were taken at 0.5 T, where WAL contributes little to the resistance. Next, $2\Delta/e$ (where we assumed the literature value of $\Delta \approx 1.4$ meV [56]) was subtracted from the total voltage, and only the voltage drop over the BSTS remains, since now the interface resistance has been removed. This was multiplied with the corresponding current to obtain the resistance of BSTS (R_{BSTS}) in the junction. Again it was found that BSTS does not scale with the length of the junction, since no fit through the origin can be found within the (large) uncertainty of the junction length.

Although it is tempting, it is not correct to subtract these values of R_{BSTS} from the resistances shown in Figure 5.5, to obtain the interface resistances. These resistances where measured on the ZBRP where EEI play a role, this is no longer the case at the higher voltages of the side peaks, so the resistance difference cannot fully be ascribed to the interface. Thus the interface resistance cannot be determined. This follows also from the adapted BTK formalism; since the interface resistance is not constant in voltage (Figure 2.3(c)). Away from the ZBRP, WAL-like behaviour is still observed, but due to the lower resistance in the absence of EEI and a much more varying resistance, it is less pronounced and no good HLN fits can be made. On the other hand, at the position of the side peaks a local interface resistance can be determined by dividing $2\Delta/e \approx 2.8$ mV by the current at these positions. Since the peaks shift to higher currents for larger junctions, the corresponding interface resistance will decrease. So the interface resistance is also not constant.

It should be noted that the minimum and maximum size of the junctions are carefully measured. If the lower boundary of junction 150 is about ten nanometers less, scaling would in principle be a possibility. Since the ears of this junction are connected, see Figure 5.9(b), it is difficult to determine the minimum length. Here it was supposed that light gray part of the ears indicate that the ears do not touch the BSTS. Furthermore the connection of the ears could also be an explanation for the observed broad dip around zero field, see Figure 5.1(b,c). A weak link of ears, as discussed in the previous chapter, together with a S-pS-N-pS-S junction could explain this feature.

5.4 Discussion and outlook

More measurements have to be performed to fully understand the origin of the peaks in the samples. In the first place it is interesting to make (long) resistive Nb-BSTS-Nb junctions of exactly the same dimensions on different positions of the BSTS. In this way one is able to verify if the conductivity is indeed very inhomogeneous in the BSTS. If this is indeed the case, then one should try to realize BSTS samples with a uniform conductivity, in order to do a scaling analysis and determine the interface resistance. Then, one should redo the measurements and make proper fits for EEI and WAL (or both) to the data. Temperature dependent measurements could improve this analysis, because it makes an extra verification possible by fitting the full temperature dependence of WAL and EEI.

A particular relevant experiment would be measuring the resistive junctions in a parallel magnetic field. Now due to the expected 2D nature of the WAL, it should not be present anymore. This can be used as a verification that indeed WAL is observed in the current data. Only a 3D contribution could still be present, but since the flakes are very thin (in the order of L_ϕ), this is not expected. If this would be present it could be subtracted from the perpendicular resistance [59], and perhaps result in a better fit of the HLN equation.

We are already working on Au-BSTS-Nb junctions, in which the absence of a gap in gold makes it easier to probe the BSTS and determine whether or not the ZBRP is intrinsic to BSTS or linked to the S-TI-S system. From this system it is easier to explain the results in terms of density of states of the (induced superconducting) BSTS. Ideally, one only wants

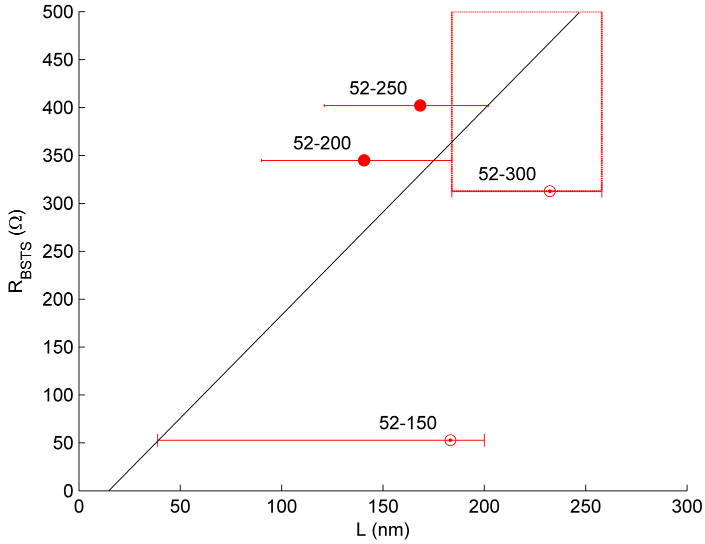

(a)

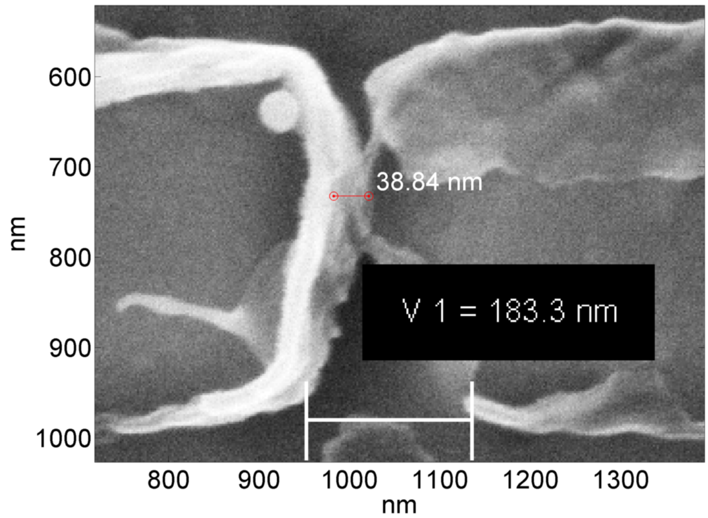

(b)

Figure 5.9: (a) The resistance of BSTS in the junctions of sample 52, calculated from the observed side peaks, assuming these are due to pSN junctions. Open dots indicates that either the junction is very rough (52-100) or that no side peaks are observed in the range of the measurement (52-300). Red lines indicate the error region. The black line indicates the minimal slope that can be obtained. (b) Junction 150 with the measurement of the lower error bar boundary (red line).

to have the induced superconducting BSTS connected to the Au separated between some kind of barrier (i.e. $Z \neq 0$). This would reduce the relative contribution of EEI and WAL effects and makes it possible to clearly observe the side peaks and to determine whether or not p-wave superconductivity is induced (also indicated by a subgap peak in the conductivity due to Andreev reflection).

Up till now tentative results of these experiments still show a ZBRP and it has qualitatively the same behaviour as the junctions discussed in this chapter. Temperature dependent measurements indicate that the central ZBRP decreases with temperature, whereas the side peaks do less. This underlines the explanations of EEI for the ZBRP and gap edges for the side peaks.

Additionally, is it also interesting to do measurements with the LIA on resistive (long) Nb-[normal metal]-Nb junction to see if the side peaks are indeed opposed in a s-wave superconductor, as is expected from the BTK theory. This way one can exclude the possibility that the peaks are the reaction of the LIA on a discontinuity in the density of states.

If it is certain that p-wave superconductivity is induced it would be interesting to reduce the normal BSTS part in a SNS junction by such an amount that Andreev Bound states appear. Measuring the AC Josephson effect (Shapiro steps) could then show indications of Majorana fermions in this system, but only for perpendicular channels (see [30] for a discussion).

5.5 Conclusions

Junctions with a designed length of 150, 200, 250 and 300 nm were resistive and showed a Zero Bias Resistance Peak (ZBRP). We attribute this ZBRP to electron-electron interactions (EEI) in the 2D surface states. In the magnetoresistance a minimum at zero field was observed, most clearly seen at the ZBRP, we ascribed this to WAL (perhaps in combination with EEI). The HLN fits to the relative magnetoconductivity give large deviation of (especially) the α-value within the same sample. This indicates that the magnetoresistance does not scale with the junction length; this might be due to the impossibility of determining the Nb-BSTS interface resistance, an inhomogeneity of the conductivity of BSTS, the difficulty of determining the exact junction area because of ears, or a combination of them.

Side peaks were observed in some samples. It was speculated that they might be indications of p-wave superconductivity in an induced S-pS-N-pS-S junction. The peaks are not always at the same gap position, but at larger voltages, this might be due to the voltage drop over the BSTS. Also from these peaks it follows that BSTS is likely to be very inhomogeneous with respect to the conductivity.

Further research has to be carried out to verify these proposals. For that some options were suggested.

Chapter 6

Transport measurements on $Cu_{0.3}Bi_{2.1}Se_3$

6.1 Goal

Measurements on a bulk $Cu_{0.3}Bi_{2.1}Se_3$ crystal, performed by the 'Quantum Electron Matter' group of the University of Amsterdam, showed that the $Cu_{0.3}Bi_{2.1}Se_3$ crystal was superconducting. The principal goal of this project was measuring whether or not also cleaved flakes of the provided $Cu_{0.3}Bi_{2.1}Se_3$ were superconducting.

6.2 Characterization and measurements

The measurements were carried on in the liquid helium bath cryostat of our group, at zero magnetic field and at temperatures around 1.5 K, well below T_c. A four-point measurement was carried out, and the resulting I, V-graphs were displayed on an analogue oscilloscope. In total eight samples were measured, none of them showed sign of superconductivity: all I, V-graphs were linear curves from which we calculated the resistances: the typical resistance was in the order of 1 Ω (in the range from 0.4 to 4 Ω).

According to [17] the cleaved flakes turn golden instead of silvery shining after one day of exposure to air. They suggest minimizing the exposure to air, but the effect of air exposure on the quality of the crystal is not discussed. To our knowledge, we did not observe this effect. During the processing it was impossible to avoid contact with air, but the flakes were shortly etched before depositing the gold leads (as discussed in Chapter 3). Therefore, it is not expected to have an oxidized surface underneath the leads. The crystal was also still superconducting when measured afterwards by the University of Amsterdam. Thus, it is not expected that the exposure to air had any influence on the results.

6.3 Results, conclusions and further work

Before and after our measurements, the I, V characteristics of the bulk crystal were measured by the University of Amsterdam. They observed superconductivity both times. So, although the crystal as a whole is superconducting, thin flakes from this crystal are not. This is an indication that the CBS crystal might not be uniformly doped with Cu^{1+} by intercalation, leading to the existence of superconducting and non-superconducting areas. Since eight flakes were measured to be not superconducting, this indicates that the superconducting volume fraction is probably quite small. Another probability is that the non-superconducting parts of the crystal cleave more easily, which could explain the difficulty to cleave large flakes as discussed in Chapter 3, although this is (to our knowledge) never mentioned in the literature for other experiments with CBS flakes.

Further research should focus on determining the superconducting volume fraction and trying to increasing it. This can be done by local probing the crystals' surface with 'point-contact Andreev reflection spectroscopy', as was done by Chen et al. [19], but now redo the experiment after cleaving the just measured surface. Furthermore it is important to determine whether or not CBS is a topological superconductor or not.

Chapter 7

Conclusions and recommendations

7.1 Conclusions

Junctions of the superconductor niobium (Nb) and the topological insulator $Bi_{1.5}Sb_{0.5}Te_{1.7}Se_{1.3}$ (BSTS) have been made. The niobium is deposited on a BSTS flake by a combination of photolithography, e-beam lithography and standard sputtering techniques. The manufacturing turned out to be quite challenging. The realized and measured junctions had a designed length of 50, 100, 150, 200, 250 and 300 nm, but due to an overexposure in the e-beam procedure the junctions were much smaller.

Four-point transport measurements on two samples with Nb-BSTS-Nb junctions were performed at low temperatures. No superconductivity was measured in these junctions for temperatures down to 1.5 K. In the Triton dilution refrigerator, operating at temperatures down to 20 mK and magnetic fields up to 3 T, supercurrents through the two smallest junctions were observed in both samples 49 and 52. After the measurements, SEM images revealed that these superconducting junctions were shorts of niobium (ears), forming weak links of Nb ears or microbridges. The observed Fraunhofer modulation can be assigned to these hybrid structures. Due to the niobium weak links, the shunted capacitance of the junction is too low to explain the observed hysteresis in the I, V-curves (and differential resistance). This hysteresis is likely due to electron heating (hot electrons).

The other four junctions on both samples, measured under the same circumstances, were not superconducting. Instead, we observed a Zero Bias Resistance Peak (ZBRP). We attribute this ZBRP to 2D electron-electron interactions (EEI) (in the 2D surface states). In the magnetoresistance a minimum at zero magnetic field was observed, which was especially pronounced at the ZBRP. We ascribed this to weak antilocalization (WAL) (perhaps in combination with electron-electron interactions (EEI)). Fits of the 2D Hikami-Larkin-Nagaoka (HLN) equation to the relative magnetoconductivity of the junctions, resulted in a large deviation of (especially) the α-values within the same sample. This indicates that the magnetoresistance does not scale with the junction length. This might be due to the impossibility of determining the Nb-BSTS interface resistance, an inhomogeneity of the conductivity of BSTS, the difficulty of determining the exact junction area due to ears, or a combination of these factors.

Side peaks were observed in some of the junctions on sample 52. It was speculated that these might be indications of p-wave superconductivity in an induced S-pS-N-pS-S junction. The peaks are however not always at the same gap position, but at larger voltages, this might be due to the voltage drop over the BSTS. From the side peaks the resistance of BSTS was calculated, again BSTS did not scale with the junction length, indicating inhomogeneity in BSTS with respect to the conductivity. Further research is needed to verify these proposals, for which some suggestions were presented.

Two other series of samples were also fabricated. One set consisted of Au-BSTS-Nb junctions, which are still under study. The manufacturing of this set of samples is comparable to the Nb-BSTS-Nb junctions. The other set of samples consisted of gold contacts on flakes of the topological superconductor $Cu_{0.3}Bi_{2.1}Se_3$ (CBS). The gold contacts were deposited by photolithography and RF sputtering. The cleaving of this crystal is much harder than the cleaving of BSTS crystal and the resulting flakes are generally smaller and thicker. Moreover, successful gold lift-off is difficult. Therefore, the production of these samples is challenging.

We did four-point transport measurements at 1.5 K, on eight samples with thin flakes of $Cu_{0.3}Bi_{2.1}Se_3$. Instead of superconductivity, resistances were measured in the order of 1Ω. However, at the University of Amsterdam superconductivity was measured on the bulk crystal before and after our experiments. So, although the crystal as a whole is superconducting, thin flakes from this crystal are not. This is an indication that the CBS crystal might not be uniformly doped with Cu^{1+} by intercalation, which results in superconducting and non-superconducting areas. Since eight flakes were found to be non-superconducting, this indicates that the superconducting volume fraction is probably quite small. Another possibility is that the non-superconducting parts of the crystal cleave more easily, which could explain the difficulty to cleave large flakes.

7.2 Recommendations and outlook

At the moment of writing, still some challenges in the manufacturing of the devices have to be overcome in the future. In image reversal photolithography bubbles are sometimes formed, after the first exposure. These bubbles are most likely due to the degassing of nitrogen from the photoresist during exposure. Several solutions are proposed in [50]. However, since the recipe gave good results in the past and was not changed, it is assumed that the new wafers cause the problems. To have a reasonable success rate in manufacturing samples it is necessary to solve this problem.

This success rate, the quality of the samples with topological insulators and the time spent on making them, will also be highly improved if it becomes possible to grow high quality layers of BSTS and CBS. A few groups worldwide are able to grow BSTS, already. In this way, junctions can be written first on a suitable insulator, ears can be easily removed without the risk of removing the flake and the dimensions can be checked with SEM before measurements. Finally, a topological insulator can be grown on top. In this way, small junctions of less than the normal coherence length of BSTS at 2 K ($\xi_n \approx 30.5$ nm) can be realized easily. This allows one to do measurements at higher temperatures or easier measure (larger) supercurrents.

As long as growing is not possible, it is interesting to optimize the properties of BSTS further. In order to get a large insulating bulk, the disorder in BSTS due to charged defects was increased by tuning its composition to maximal bulk resistivity. Disorder decreases the mean free path. It would be interesting to find a good compromise between optimal bulk resistivity and optimal mean free path, by tuning the composition. A larger mean free path of BSTS, gives rise to a larger normal coherence length which makes it able to work with larger junctions or at higher temperatures.

A last point with regard the success rate concerns the use of the SEM. In the present case SEM images were made after all measurements series in order to protect our samples. Since Josephson effects were measured it was not expected that the junction were not good. Therefore, considering the time it takes to make, measure and analyze the measurement of the samples, it might be worthwhile to investigate if SEM really has a large impact on the quality of the BSTS. If PMMA resist is on top of the sample during SEM the BSTS might be protected enough.

With regard to the resistive Nb-BSTS-Nb junctions, it is recommended to do further experiments in order to have a better understanding of the observed peaks. A particular relevant experiment would be measuring the resistive junctions in a parallel magnetic field. In this configuration WAL should not be present anymore, due to the expected 2D nature of the WAL. This could be used to verify that WAL is indeed observed in the current data. Only a 3D contribution could still be present, but since the flakes are very thin (in the order of L_ϕ), this is not expected. If 3D contributions would still be present they could be subtracted from the perpendicular resistance, which would perhaps result in a better fit of the HLN equation [59].

It is also interesting to make (long) resistive Nb-BSTS-Nb junctions of exactly the same dimensions on different positions of the BSTS. In this way one is able to verify if the conductivity is indeed very inhomogeneous in BSTS. If this is so, then one should try to realize BSTS samples with a uniform conductivity, in order to do a scaling analysis and determine the interface resistance. Then, redo the measurements and make proper fits for EEI and WAL (or both) to the data. Temperature dependent measurements could improve this analysis, because it enables an extra verification by fitting the full temperature dependence of WAL and EEI.

We started already working on Au-BSTS-Nb junctions, in which the absence of a superconducting gap in the gold electrode, makes it easier to probe the BSTS and determine whether or not the ZBRP is intrinsic to BSTS or linked to the S-TI-S system. From this system it is easier to explain the results in terms of density of states of the (induced superconducting) BSTS. Ideally, one would only like to have the induced superconducting BSTS connected to the Au separated between some kind of barrier. This would reduce the possible EEI and WAL effects and makes it possible to clearly observe the side peaks and to determine whether or not p-wave superconductivity is induced (which is also indicated by a subgap peak in the conductivity due to Andreev reflection).

Up till now tentative results of these experiments still show a ZBRP and reveal qualitatively the same behaviour as the junctions discussed in this thesis. Temperature dependent measurements have shown that the central ZBRP depends on temperature, while the side peaks do less. This underlines the explanations of EEI for the ZBRP and gap edges for the side peaks.

Additionally, is it also interesting to do measurements with the LIA on resistive (long) Nb-[normal metal]-Nb junction to see if the side peaks are indeed opposite in a s-wave superconductor, as is expected from the BTK theory. This would exclude the possibility that the peaks are the reaction of the LIA on a discontinuity in the density of states.

If it is certain that p-wave superconductivity is induced it would be interesting to reduce the normal BSTS part in a SNS junction by such an amount that Andreev Bound states appear. Measuring the AC Josephson effect (Shapiro steps) could then show indications of Majorana fermions in this system, but only for perpendicular channels (see [30] for a discussion).

Finally, further research regarding CBS should focus on determining the superconducting volume fraction and trying to increasing it. This can be done by locally probing the crystals' surface with 'point-contact Andreev reflection spectroscopy', as was done by Chen et al. [19], but now redo the experiment after cleaving the just measured surface. Furthermore, it is important to determine whether or not CBS is a topological superconductor or not.

Dankwoord

Ruim negen maanden geleden begon ik aan het avontuur dat afstuderen heet, het was een mooie enerverende tijd, waarin ik veel heb geleerd. De prettige sfeer in de vakgroep heeft daar zeker aan bijgedragen. Ik ben iedereen in de vakgroep ICE/QTM niet alleen dankbaar voor hun behulpzaamheid, maar ook voor alle gezelligheid.

Een aantal mensen wil ik hier in het bijzonder danken. Op de eerste plaats is dat natuurlijk Marieke, mijn dagelijkse begeleider, ik heb veel van je geleerd, bedankt voor de samenwerking en al je hulp! Cor, bedankt voor je hulp bij de lage temperatuurmetingen en je bereidheid om altijd te helpen bij vragen en problemen. Ik wil jou, Sam en Roel daarnaast bedanken voor de gezelligheid in ons kantoor. Frank en Dick, bedankt voor de ondersteuning in het lab, de introducties op de apparatuur en het meedenken bij de productieproblemen van de samples. Verder wil ik Elia van de Nano Electronics groep bedanken voor zijn ondersteuning bij de metingen in de Triton. Zeker niet in de laatste plaats, wil ik Alexander bedanken voor zijn motiverende enthousiasme en al zijn hulp, maar ook dat ik mocht afstuderen in 'zijn' Topoteam. Ook wil ik Stefan bedanken voor zijn bereidheid om zitting te nemen in mijn afstudeercommissie.

Verder wil ik hierbij van de gelegenheid gebruik maken om mijn familie te bedanken voor hun interesse in mijn Natuurkundestudie. In het bijzonder ben ik veel dank verschuldigd aan mijn ouders die mijn studie medemogelijk hebben gemaakt en me altijd hebben ondersteund.

Nu ik mijn studietijd in Enschede hierbij zo goed als afrond, kijk ik terug op een mooie tijd, waarvoor ik niet alleen mijn vrienden en studiegenoten dank verschuldigd ben, maar zeker ook de redactie van de Focus en mijn commissiegenootjes van de ICPS. Helaas komt ook aan al het goede een eind, maar elk eind is ook een nieuw begin, ik zie dan ook uit naar mijn volgende uitdaging!

Thijs

Bibliography

[1] Kane, C.L., and E.J. Mele, *Quantum Spin Hall Effect in Graphene*, Phys. Rev. Lett., 2005, Vol. 95, p. 226801

[2] Qi, X.-L., and S.-C. Zhang, *Topological insulators and superconductors*, Rev. Mod. Phys., 2011, Vol. 83, p. 1057

[3] Fu, L., and C.L. Kane, *Superconducting Proximity Effect and Majorana Fermions at the Surface of a Topological Insulator*, Phys. Rev. Lett., 2008, Vol. 100, p. 096407

[4] Hasan, M.Z., and C.L. Kane, *Colloquium: Topological insulators*, Rev. Mod. Phys., 2010, Vol. 92, p. 3045

[5] Leijnse, M., and K. Flensberg, *Introduction to topological superconductivity and Majorana fermions*, Semicond. Sci. Technol., 2012, Vol. 27, p. 124003

[6] Hoek, M., *Coupling a Superconductor to a Topological Insulator*, Master Thesis, 2010, University of Twente, Enschede, The Netherlands

[7] Snelder, M., *Towards topological insulator devices for the creation of Majorana fermions*, Master Thesis, 2011, University of Twente, Enschede, The Netherlands

[8] Veldhorst, M., M. Snelder, M. Hoek, T. Gang, V.K. Guduru, X.L. Wang, U. Zeitler, W.G. Van der Wiel, A.A. Golubov, H. Hilgenkamp, and A. Brinkman, *Josephson supercurrent through a topological insulator surface state*, Nature Materials, 2012, Vol. 11, p. 417

[9] Ando, Y., *Topological Insulator Materials*, unpublished, 2013, arXiv:1304.5693

[10] Qu, D.-X., Y.S. Hor, J. Xiong, R.J. Cava, and N.P. Ong *Quantum Oscillations and Hall Anomaly of Surface States in the Topological Insulator Bi_2Te_3*, Science, 2010, Vol. 329, p. 821

[11] Taskin, A.A., Z. Ren, S. Sasaki, K. Segawa, and Y. Ando, *Observation of Dirac Holes and Electrons in a Topological Insulator*, Phys. Rev. Lett., 2011, Vol. 107, p. 016801

[12] Ren, Z., A.A. Taskin, S. Sasaki, K. Segawa, and Y. Ando, *Optimizing $Bi_{2-x}Sb_xTe_{3-y}Se_y$ solid solutions to approach the intrinsic topological insulator regime*, Phys. Rev. B, 2011, Vol. 84, p. 165311

[13] Xia, B., P. Ren, A. Sulaev, P. Liu, S.Q. Shen, and L. Wang, *Indications of surface-dominated transport in single crystalline nanoflake devices of topological insulator $Bi_{1.5}Sb_{0.5}Te_{1.8}Se_{1.2}$*, Phys. Rev. B, 2013, Vol. 87, p. 085442

[14] Qi, X-L., and S-C. Zhang, *The quantum spin Hall effect and topological insulators*, Phys. Today, 2010, Vol. 63, Issue 1, p. 33

[15] Veldhorst, M., M. Snelder, M. Hoek, C.G. Molenaar, D.P. Leusink, A.A. Golubov, H. Hilgenkamp, and A. Brinkman, *Magnetotransport and induced superconductivity in Bi based three-dimensional topological insulators*, Phys. Status Solidi RRL, 2012, p. 1

[16] Segawa, K., Z. Ren, S. Sasaki, T. Tsuda, and Y. Ando, *Ambipolar transport in bulk crystals of a topological insulator by gating with ionic liquid*, Phys. Rev. B, 2012, Vol. 86, p. 075306

[17] Hor, Y.S., A.J. Wiliams, J.G. Checkelsky, P. Roushan, J. Seo, Q. Xu, H.W. Zandbergen, A. Yazdami, N.P. Ong, and R.J. Cava, *Superconductivity in $Cu_xBi_2Se_3$ and its Implications for Pairing in the Undoped Topological Insulator*, Phys. Rev. Lett., 2010, Vol. 104, p. 057001

[18] Bay, T.V., T. Naka, Y.K. Huang, H. Luigjes, M.S. Golden, and A. de Visser, *Superconductivity in the Doped Topological Insulator $Cu_xBi_2Se_3$ under High Pressure*, Phys. Rev. Lett., 2012, Vol. 108, p. 057001

[19] Chen, X., C. Huan, Y.S. Hor, C.A.R. Sá de Melo, and Z. Jiang, *Point-contact Andreev reflection spectroscopy of candidate topological superconductor $Cu_{0.25}Bi_2Se_3$*, unpublished, 2012, arXiv:1210.6054v1

[20] Fu, L., and E. Berg, *Odd-Parity Topological Superconductors: Theory and Application to $Cu_xBi_2Se_3$*, Phys. Rev. Lett., 2010, Vol. 105, p. 097001

[21] Peng, H., D. De, B. Lv, F. Wei, and C.-W. Chu, *Absence of zero-energy surface bound states in $Cu_xBi_2Se_3$ via a study of Andreev reflection spectroscopy*, unpublished, 2013, arXiv:1301.1030v1

[22] Cyrot, M., and D. Pavuna, *Introduction to Superconductivity and High-Tc Materials*, 1992, World Scientific, Singapore

[23] Poole, C.P., H.A. Farach, R.J. Creswick and R. Prozorov, *Superconductivity*, second edition, 2007, Academic Press, London, UK

[24] Blonder G.E., M. Tinkham, and T.M. Klapwijk, *Transition from metallic to tunneling regimes in superconducting microconstrictions: Excess current, charge imbalance, and supercurrent conversion*, Phys. Rev. B, 1982, Vol. 25, p. 4515

[25] Eschrig, M., C. Iniotakis, and Y. Tanaka, *Theoretical aspects of Andreev spectroscopy and tunneling spectroscopy in non-centrosymmetric superconductors: a topical review*, unpublished, 2010, arXiv:1001.2486v1

[26] Xiao-Wei, L.I., *Tunneling Conductance in Normal Metal/Insulator/Triplet Superconductor Junction*, Commun. Theor. Phys., 2005, Vol. 44, p. 381

[27] Harmans, C., *Mesoscopic Physics, an introduction*, 2003, Lecture Notes, TU Delft, The Netherlands, online: http://ocw.tudelft.nl/courses/nanoscience/ mesoscopic-physics/course-home/

[28] Mourik, V., K. Zuo, S.M. Frolov, S.R. Plissard, E.P.A.M. Bakkers, and L.P. Kouwenhoven, *Signatures of Majorana Fermions in Hybrid Superconductor-Semiconductor Nanowire Devices*, Science, 2012, Vol. 336, p. 1003

[29] Pillet, J.-D., C.H.L. Quay, P. Morfin, C. Bena, A.L. Yeyati, and P. Joyez, *Andreev bound states in supercurrent-carrying carbon nanotubes revealed*, Nat. Phys., 2010, Vol. 6, p. 965

[30] Snelder, M., M. Veldhorst, A.A. Golubov, and A. Brinkman, *Andreev bound states and current-phase relations in three-dimensional topological insulators*, Phys. Rev. B, 2013, Vol. 87, p. 104507

[31] Weisstein, Eric W., *Topology*, from MathWorld - A Wolfram Web Resource, http://mathworld.wolfram.com/Topology.html, visited: 05-11-12

[32] Datta, S., *Electronic transport in mesoscopic systems*, 1995, Cambridge University Press, Cambridge, United Kingdom

[33] Zhang, H., C.-X. Liu, X.-L. Qi, X. Dai, Z. Fang, and S.-C. Zhang, *Topological insulators in Bi_2Se_3, Bi_2Te_3 and Sb_2Te_3 with a single Dirac cone on the surface*, Nat. Phys., 2009, Vol. 5, p. 438

[34] Beenakker, C.W.J., *Search for Majorana fermions in superconductors*, unpublished, 2012, arXiv:1112.1950

[35] Alicea, J., *New directions in the pursuit of Majorana fermions in solid state systems*, Rep. Prog. Phys., 2012, Vol. 75, 076501

[36] Williams, J.R., A.J. Bestwick, P. Gallagher, S.S. Hong, Y. Cui, Andrew S. Bleich, J.G. Analytis, I.R. Fisher, and D. Goldhaber-Gordon, *Unconventional Josephson Effect in Hybrid Superconductor-Topological Insulator Devices*, Phys. Rev. Lett., 2012, Vol. 109, p. 056803

[37] Jiang, L., D. Pekker, J. Alicea, G. Refael, Y. Oreg, and F. von Oppen, *Unconventional Josephson Signatures of Majorana Bound States*, Phys. Rev. Lett., 2011, Vol. 107, p. 236401

[38] Wiliams, J.R., and D. Goldhaber-Gordon, *Doubling down on Majorana*, Nat. Phys., 2012, Vol. 8, p. 778

[39] Veldhorst, M., C.G. Molenaar, C.J.M. Verwijs, H. Hilgenkamp, and A. Brinkman, *Optimizing the Majorana character of SQUIDs with topologically nontrivial barriers*, Phys. Rev. B, 2012, Vol. 86, p. 024509

[40] Ghantmakher, V.F., *Electrons and Disorder in Solids*, 2005, Oxford University Press, Oxford

[41] Akkermans, E., and G. Montambaux, *Mesoscopic Physics of Electrons and Photons*, 2007, Cambridge University Press, Cambridge, United Kingdom

[42] Liu, M., J. Zhang, C.-Z. Chang, Z. Zhang, X. Feng, K. Li, K. He, L.-L. Wang, X. Chen, X. Dai, Z. Fang, Q.-K. Xue, X. Ma, and Y. Wang, *Crossover between Weak Antilocalization and Weak Localization in a magnetically doped topological insulator*, Phys. Rev. Lett., 2012, Vol. 108, p. 036805

[43] Hikami, S., A. Larkin, and Y. Nagaoka, *Spin-Orbit Interaction and Magnetoresistance in two dimenional random systems*, Prog. Theor. Phys., 1980, Vol. 63, p. 707

[44] Lee, P.A., and T.V. Ramakrishnan, *Disordered electronic systems*, Rev. Mod. Phys., 1985, Vol. 57, p. 287

[45] Wang, J., A.M. DaSilva, C.-Z. Chnag, K. He, J.K. Jian, N. Samarth, X.-C. Ma, Q.-K. Xue, and M.H.W. Chan, *Evidence for electron-electron interaction in topological insulator thin films*, Phys. Rev. B, 2011, Vol. 83, p. 245438

[46] Beutler, D.E., and N. Giordano, *Localization and electron-electron interaction effects in thin Bi wires and films*, Phys. Rev. B, 1988, Vol. 38, p. 8

[47] Liu, M., C.-Z. Chang, Z. Zhang, Y. Zhang, W. Ruan, K. He, L.-L. Wang, X. Chen, J.-F. Jia, S.-C. Zhang, Q.-K. Xue, X. Ma, and Y. Wang, *Electron interaction-driven insulating ground state in Bi_2Se_3 topological insulators in the two-dimensional limit*, Phys. Rev. B, 2011, Vol. 83, p. 165440

[48] More details of the FIB can be found at `http://www.utwente.nl/mesaplus/nanolab/Archive/equipment/materials%20characterization/108.%20Dual-FIB%20FEI%20Instruments/`, visited: 5 May 2013

[49] Koren, G., and T. Kirzhner, *Zero-energy bound states in tunneling conductance spectra at the interface of an s-wave superconductor and a topological insulator in NbN/Bi_2Se_3/Au thin-film junctions*, Phys. Rev. B, 2012, Vol. 86, p. 144508

[50] MicroChemicals, *Lithography Trouble Shooter*, 2012, `http://sindhu.ece.iisc.ernet.in/nanofab/twikii/pub/Main/Lithography/Lithography%20TroubleShooter_Microchem.pdf`, visited: 7 May 2013

[51] Qu F., F. Yang, J. Shen, Y. Ding, J. Chen, Z. Ji, G. Liu, J. Fan, X. Jing, C. Yang, and L. Lu, *Strong Superconducting Proximity Effect in Pb-Bi_2Te_3 Hybrid Structures*, Sci. Rep., 2012, Vol. 2:339

[52] Courtois, H., M. Meschke, J.T. Peltonen, and J.P. Pekola, *Origin of Hysteresis in a Proximity Josephson Junction*, Phys. Rev. Lett., 2008, Vol. 101, p. 067002

[53] Tinkham, M., *Introduction to Superconductivity*, second edition, 1996, McGraw-Hill, USA

[54] Uchida, N., K. Enpuku, Y. Matsugaki, S. Tomita, F. Irie, and K. Yoshida, *Flux trapping in Josephson tunnel junctions*, J. Appl. Phys., 1983, Vol. 54, Issue 9, p. 5287

[55] Aslamazov, L.G., and A.I. Larkin, *Josephson effect in wide superconducting bridges*, Zh.Eksp.Teor.Fiz., 1975, Vol. 68, p. 766

[56] Brinkman, A., *Charge transport in double-barrier and magnesiumdiboride Josephson junctions*, PhD Thesis, 2003, University of Twente, Enschede, The Netherlands

[57] Van Duzer, T., and C.W. Turner, *Principles of Superconductive Devices and Circuits*, chapter 4, second edition, 1999, Pearson Education/Prentice Hall, USA

[58] Lam, S.K.H., *Proximity effect on vortex dynamics at low field in Nb and Nb-Au bilayer microbridges exhibiting strong pinning*, J. Appl. Phys., 2011, Vol. 110, p. 063919

[59] Hollanders, S., *Exploratory research of the 3D topological insulator $Bi_{1.5}Sb_{0.5}Te_{1.3}Se_{1.7}$ by means of magnetotransport*, Master Thesis, 2012, University of Amsterdam/Van der Waals-Zeeman Institute, Amsterdam, The Netherlands

Appendix A

Lithography recipes

A.1 Positive lithography

For the 'normal' positive lithography the following recipe was used:

- Pre-bake at 100°C for 2 minutes (remove vapor from surface);
- Spin 1.7 µm photoresist with POS6000 program;
- Bake the sample at 100°C for 1 minute (hardening of the photoresist);
- Align a positive mask on the flake and do a 5 seconds UV exposure (hard contact);
- Develop the sample in OPD4262 for 60 seconds and wash two times in demiwater for 30 seconds.

A.2 Image reversal lithography

For the image reversal lithography the following recipe was used:

- Pre-bake at 100-120°C for 2 minutes (remove vapor from surface);
- Spin HMDS (for better photoresist adhesion) - 4.000 RPM for 30 seconds;
- Spin Ti35ES (3.5 µm) image reversal photoresist - 4.000 RPM for 45 seconds;
- Bake the sample at 100°C for 2 minutes ('drying' of the photoresist);
- Align a negative mask on the flake and do a 23 seconds UV exposure (hard contact);
- Wait (at least) 20 minutes (time for photoresist to degas N_2);
- Bake the sample at 120°C for 2 minutes;
- Wait (at least) 5 minutes (time for photoresist to degas N_2);
- UV flood exposure for 1 minute for image reversal;
- Develop the sample in OPD4262 for 55±5 seconds and wash two times in demiwater for 30 seconds.

Possible improvements to overcome bubble formation are: a longer softbake (at least 3.5 minutes after spinning), cleaning the sample carefully in acetone and isopropyl alcohol before starting the whole procedure and using a less intense exposure.

A.3 E-beam lithography

For the e-beam lithography the following recipe was used:

- Pre-bake at 100-120°C for 2 minutes (remove vapor from surface);
- Spin 298 nm PMMA A4 resist - 3.000 RPM for 45 seconds;
- Bake the sample at 160°C for 5 minutes ('drying' of the photoresist);
- Scratch marker on the sample, load samples and calibrate the beam;
- Write the digital mask with e-beam at 10 kV acceleration voltage, 10 µm aperture, a working distance of 10 mm and a dose of about 140 $\mu C/cm^2$;
- Develop the sample in a solution of MIBK:IPA for 30 seconds followed by 30 seconds in a IPA stopper solution.

PMMA = polymethyl methacrylate; MIBK = methyl isobutyl ketone; IPA = isopropanol.

Appendix B

Deposition schemes

B.1 Pd/Nb deposition

Optimized DC and RF sputtering conditions of Pd/Nb in Nordiko			
Date	19-04-2013		
Process	substrate cleaning - presputtering - sputtering deposition		
• **RF substrate cleaning**			
Q_{RF} (W)	55	Ar (ml/min)	55.4
V (V)	300	time (min)	1
P_{conv} (mbar)	$1.33 \cdot 10^{-2}$		
• **Pd (RF)/Nb (DC) presputter at large shutter**			
Q_{DC} (W)	700/250	Ar (ml/min)	54/28.4
V_{DC} (V)	1400/331	time (min)	5/3
P_{conv} (mbar)	$1.33/0.73 \cdot 10^{-2}$	I_{DC} (A)	-/0.73
• **Nb (DC) presputter at small shutter**			
Q_{DC} (W)	250	I_{DC} (A)	0.73
V_{DC} (V)	340	time (min)	4
• **Nb (DC)/Pd (RF) deposition**			
Q_{DC} (W)	250/700	I_{DC} (A)	0.73/-
V_{DC} (V)	341/1400	time	2.5 min./7 sec.
rate (nm/min)	80/20	d (nm)	200/2.3
Ion gauge chamber pressure before	$< 2 \cdot 10^{-7}$		

Table B.1: Optimized sputtering conditions of Pd/Nb in Nordiko, most samples were fabricated in a slightly different sequence: first all Nb steps, followed by the Pd steps. This optimized process scheme is more time-efficient and reduces the time between the deposition of Pd and Nb, in order to reduce the change of oxidation even more.

B.2 Au deposition

Optimized RF sputtering conditions of Ti/Au in Perkin Elmer				
Process	Ti target cleaning - substrate etch - Ti deposition - Au deposition			
P_{Ar} (mbar)	$2 \cdot 10^{-2}$			
Ti target cleaning	P (W)	250	Time (min)	2
substrate etching	P (W)	150	Time (min)	2
Ti deposition	P (W)	150	Time (min)	0.5
Au deposition	P (W)	150	Time (min)	3

Table B.2: Conditions for Ti/Au sputtering

Appendix C

Fraunhofer modulation

The dc Josephson current I_0 (at zero magnetic field) can be suppressed in a magnetic field B, resulting in a Fraunhofer like modulation of the critical current I. This modulation can be described by a sinc-function:

$$I(B) = I_0(0) \left| \frac{\sin(\pi\phi_B/\alpha\phi_0)}{\pi\phi_B/\alpha\phi_0} \right| \tag{C.1}$$

with $\phi_0 = \frac{h}{2e} \approx 2.0678 \cdot 10^{-15}$ Wb and $\alpha = 2$ for topological insulators. While the magnetic flux ϕ_B trough the effective junction area A can be expressed by:

$$\phi_B = \iint \vec{B} \cdot \mathrm{d}\vec{a} = BA = BWL' \text{ (in perpendicular magnetic field)}, \tag{C.2}$$

with W the junction width and $L' = L + 2\lambda$ the effective junction length, consisting of the junction length L and the penetration depth of the magnetic field into the superconductor. The case $I = 0$ holds if

$$\frac{\pi\phi_B}{\alpha\phi_0} = n\pi \neq 0 \Rightarrow \phi_B = \alpha n \phi_0 \ (n = 1, 2, 3, \ldots) \tag{C.3}$$

Then, for ΔB the difference between two zero points (the modulation), one finds from Eq. C.2

$$\Delta B = \frac{\Delta\phi_B}{A} \Rightarrow \Delta\phi_B = \Delta B A \tag{C.4}$$

and from Eq. C.3

$$\Delta\phi_B = \alpha\Delta n\phi_0 = \alpha\phi_0 \tag{C.5}$$

When setting Eq. C.4 equal to Eq. C.5, one finds the area of the Josephson junction corresponding to the Fraunhofer pattern:

$$S = \frac{\alpha\phi_0}{\Delta B} = WL' \tag{C.6}$$